Review Vol. 30, No. 3 / 31 Jan 2022 / Optics Express 4133
Optics EXPRESS

Advances in laboratory-scale ptychography using high harmonic sources [Invited]

LARS LOETGERING,[1,2,3,*] STEFAN WITTE,[4,5] AND JAN ROTHHARDT[1,2,6]

[1]Institute of Applied Physics and Abbe Center of Photonics, Friedrich Schiller University Jena, Albert-Einstein-Straße 15, 07745 Jena, Germany
[2]Helmholtz-Institute Jena, Fröbelstieg 3, 07743 Jena, Germany
[3]Leibniz Institute of Photonic Technology, Albert-Einstein-Straße 9, 07745, Jena, Germany
[4]Vrije Universiteit Amsterdam, De Boelelaan 1105, 1081 HV Amsterdam, The Netherlands
[5]ARCNL, Science Park 106, 1098 XG Amsterdam, The Netherlands
[6]Fraunhofer Institute for Applied Optics and Precision Engineering, Albert-Einstein-Straße 7, 07745 Jena, Germany
[*]lars.loetgering@uni-jena.de

Abstract: Extreme ultraviolet microscopy and wavefront sensing are key elements for next-generation ultrafast applications, such as chemically-resolved imaging, focal spot diagnostics in pump-and-probe experiments, and actinic metrology for the state-of-the-art lithography node at 13.5 nm wavelength. Ptychography offers a robust solution to the aforementioned challenges. Originally adapted by the electron and synchrotron communities, advances in the stability and brightness of high-harmonic tabletop sources have enabled the transfer of ptychography to the laboratory. This review covers the state of the art in tabletop ptychography with high harmonic generation sources. We consider hardware options such as illumination optics and detector concepts as well as algorithmic aspects in the analysis of multispectral ptychography data. Finally, we review technological application cases such as multispectral wavefront sensing, attosecond pulse characterization, and depth-resolved imaging.

1. Introduction

The ability to perform tabletop extreme ultraviolet (XUV) microscopy is a longstanding scientific challenge. Its potential is to combine the relatively short wavelength and the availability of atomic resonances across the periodic table into high-resolution, chemically-resolved imaging [1]. In addition, many modern XUV sources are controlled by ultrashort pulses, which makes them ideally suited to investigate transient phenomena at femto- and attosecond time scales, for instance by means of spectroscopic as well as pump-and-probe-type experiments [2,3]. While there exists a plethora of source concepts for the generation of XUV radiation, the principle of high harmonic generation (HHG) [4,5] arguably outperforms other techniques available to date in terms of coherent photon flux [6–8]. This in turn enables the transfer of a variety of coherent imaging techniques, which were previously available only at large-scale facilities such as synchrotrons and free-electron lasers, to laboratory-scale XUV microscopes. In particular, ptychography [9,10] is now available at compact XUV sources, as first demonstrated in the pioneering work by Seaberg et al. [11]. Ptychography is a lensless imaging technique, meaning that no imaging optics are required downstream of a sample under investigation, which considerably facilitates the experimental geometry and flux efficiency as compared to lens-based XUV microscopy setups. Moreover, it inherently exploits amplitude and phase contrast, which enables a quantitative investigation of material properties, a capability that many competing imaging techniques lack.

#443622 https://doi.org/10.1364/OE.443622
Journal © 2022 Received 23 Sep 2021; revised 4 Dec 2021; accepted 22 Dec 2021; published 25 Jan 2022

Optics EXPRESS

Early experimental demonstrations of XUV tabletop microscopy explored a variety of source as well as imaging concepts. Incoherent plasma as well as coherent XUV lasers have been used in both scanning and full field imaging modes [12–18]. The aforementioned techniques either directly recorded a magnified image of the sample, for instance using Fresnel zone plates as imaging optics, or employed a translation stage, measuring extended objects pixel by pixel by scanning it through a focused beam. While full-field and scanning microscopy are routinely applied in other spectral domains, such as the visible and near infrared region where they are found in many biomedical applications [19,20], their XUV implementation faces unique challenges. The high absorption of virtually all elements across the periodic table including air requires operation in vacuum. For the same reason, refractive imaging optics such as conventional lenses are flux inefficient and therefore not available. Instead, reflective mirrors or tailor-made diffractive optical elements (DOEs) are typically employed as objectives and condensers of XUV imaging systems. However, while reflective XUV optics tend to be flux efficient, they are challenging to fabricate at high numerical aperture and large spectral bandwidth. Vice versa, zone plates can be used for wavefront shaping and high numerical aperture focusing, but tend to have low efficiency by lack of suitable phase shifting materials in the XUV. The prevalently used binary (absorptive) DOEs are limited to an efficiency of about 10% [21]. Cascaded operation of absorptive DOEs results in excessive losses, underlining the need for lensless imaging concepts.

With the advent of coherent diffractive imaging (CDI), first demonstrated with x-rays at a synchrotron facility [22] and later at an HHG tabletop source [23], a computational lensless imaging approach became available that bypasses many of the shortcomings of lenses in the short-wavelength range. CDI may be regarded as a fundamentally different imaging paradigm as compared to lens-based techniques: instead of forming a direct, magnified image of a sample of interest, a diffraction pattern is recorded. Typically this diffraction pattern is related to the Fourier transform of the sample but lacks phase information, similar to crystallography where the electron density of a crystal is uncovered from a sequence of Bragg reflections [24]. The unknown phase information can be recovered by means of phase retrieval algorithms, provided that *a priori* knowledge about the specimen is available [25–28]. Unfortunately such *a priori* information is oftentimes either not available or not sufficient for the reconstruction of complex real-world samples. Ptychography solves this problem by measuring not a single diffraction pattern but a sequence of diffraction patterns from laterally overlapping scan positions, thus effectively overconstraining the underlying inverse problem while requiring only minimal a priori information (such as scan positions and the assumption that the beam was widely stable throughout the scan). Moreover, the large amount of data available in ptychography enables a deconvolution of the illumination beam profile and the sample under investigation. Thus the technique can jointly be used for wavefront sensing, with applications to optics characterization and focal spot diagnostics [29–33], and for quantitative absorption and phase imaging [9,10,34–39].

Within its first decade of existence, ptychography has revolutionized XUV microscopy, with an expanding application space fueled by the ever increasing flux available via HHG [40–43]. In this review we cover the principles of XUV ptychography, starting from XUV generation as well as its interaction with matter, and detector concepts (see section 2). We discuss algorithmic aspects in XUV ptychography in section 3, including wave optical considerations in transmission and reflection mode, illumination optics, multispectral operation, and practical considerations for experimental design as well as data analysis. In section 4. we consider emergent XUV applications of ptychography, wavefront sensing, pulse characterization, and routes towards 3D XUV imaging. The article closes with future opportunities and challenges in compact XUV ptychography (see section 5).

Optics EXPRESS

2. Generation, properties and detection of XUV radiation

2.1. Tabletop sources of extreme ultraviolet radiation

Extreme ultraviolet (XUV) radiation is characterized by photon energies between 30 eV and 250 eV [1]. Typical XUV tabletop sources utilize either radiation emitted by discharge- (DPP) and laser-produced (LPP) plasmas, light amplification in laser-ionized media or high harmonic generation (HHG) driven by infrared femtosecond lasers. LPP and DPP sources emit light from hot and dense plasmas covering XUV radiation up to x-ray photon energies [44–46]. Initially designed for projection lithography at 13.5 nm wavelength, these sources are nowadays employed for a wide range of metrology, imaging, and spectroscopy applications [47–51]. Although hot and dense plasmas are localized light sources, the spatial coherence of the emitted radiation is not sufficient for high-resolution lensless imaging. Narrowing of the angular emission spectrum with a simple pinhole to improve spatial coherence comes at the cost of a strongly reduced photon flux. Nevertheless, this concept has successfully been implemented and enabled ptychography in the XUV (17 nm wavelength) [50,52] and recently in the x-ray range (0.13 nm wavelength) [53] at compact radiation sources. Due to the limited coherent photon flux on the sample, the resolution achieved was only moderate: 100 nm has been achieved in the XUV and >900 nm in the x-ray experiment.

Light amplification in an excited plasma volume has been successfully employed to enable lasers in the XUV and soft x-ray spectral region [54–57]. However, the required laser pulse energies for exciting a sufficiently long plasma are of the order of 1 J, which requires high energy laser systems for pumping. Nevertheless, nanoscale imaging has been successfully demonstrated with XUV lasers [15,17,58].

The process of HHG, which was first reported in 1987 [4,5], provides an alternative route to coherent tabletop XUV radiation by frequency converting visible and infrared femtosecond laser pulses into the XUV. It usually relies on noble gases, provided by a jet, a cell or a pressurized waveguide acting as the nonlinear medium. Ionization, followed by propagation of a free electron in the strong driving laser field, and radiative recombination with the parent ion describe the basic process on a single-emitter scale [59]. In addition, phase-matching of all involved emitters in the interaction volume and re-absorption of the generated XUV radiation need to be considered to optimize the conversion efficiency of HHG. The HHG process is usually repeated at multiple half-cycles of the driving laser field resulting in the generation of odd harmonic orders. Longer driving pulses generate harmonic lines with smaller bandwidth. In contrast, few-cycle driving pulses or advanced gating techniques can restrict the emission to a single half-cycle resulting in a continuous spectrum and the generation of isolated attosecond pulses [2,60]. The highest photon energy that can be efficiently generated, the so-called *cutoff energy*, is determined by the wavelength of the driving laser, the utilized target gas, the driving laser intensity, and the phase matching conditions [60]. A typical HHG spectrum obtained with a long driving laser is shown in Fig. 1.

The conversion efficiency into a single harmonic line reaches 10^{-5} under optimized conditions [62–64]. Hence, the typical average power of HHG sources driven by a conventional watt-class titanium- sapphire-based femtosecond laser is in the μW-range, corresponding to $\sim 10^{12}$ photons/s. The available photon flux can, however, significantly be increased by employing modern high average power femtosecond lasers as drivers [41], recycling of the unconverted fundamental pulses in an enhancement cavity [43], or the generation of high-order harmonics within a femtosecond laser oscillator [65–67]. In addition, cascaded frequency conversion schemes, e.g. second or third harmonic generation in nonlinear crystals followed by high harmonic generation in noble gases, have demonstrated significantly higher conversion efficiencies [68] enabling average powers in the milliwatt range for photon energies up to 32 eV today [42]. An overview on existing high photon flux HHG sources is given in Fig. 2. Each point represents the average

Optics EXPRESS

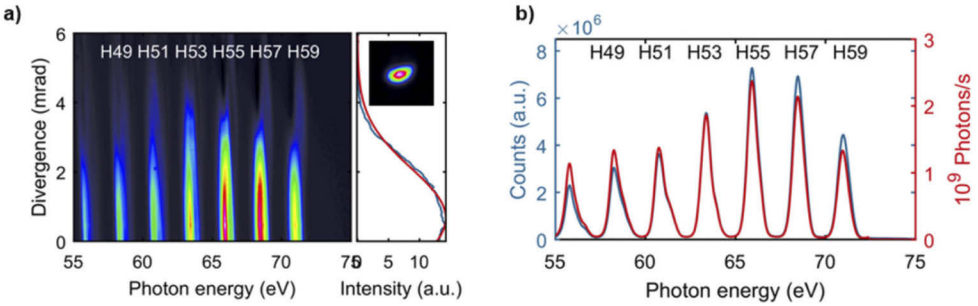

Fig. 1. Typical high harmonic spectral characteristics produced from long driving pulses. (a) Measured spatio-spectral distribution of the harmonics at optimal generation conditions (7 bar backing pressure). The HHG signal has been analyzed with an imaging spectrometer (flat-field grating) that allows observation of the divergence for each individual harmonic. The right part of (a) shows the lineout (blue) and a Gaussian fit (red) of H57 at 68.6 eV. The inset shows the focus of the XUV beam at 68.6 eV. (b) Integration along the divergence axis leads to a spatially-averaged harmonic spectrum (blue). When accounting for the detection efficiency and background absorption in the chamber a calibrated spectrum (red curve) can be obtained. Reproduced with permission from [61] © The Optical Society.

power integrated over a single harmonic line up to a photon energy of 90 eV. For larger photon energies each point represents the average power integrated within a 1 % bandwidth.

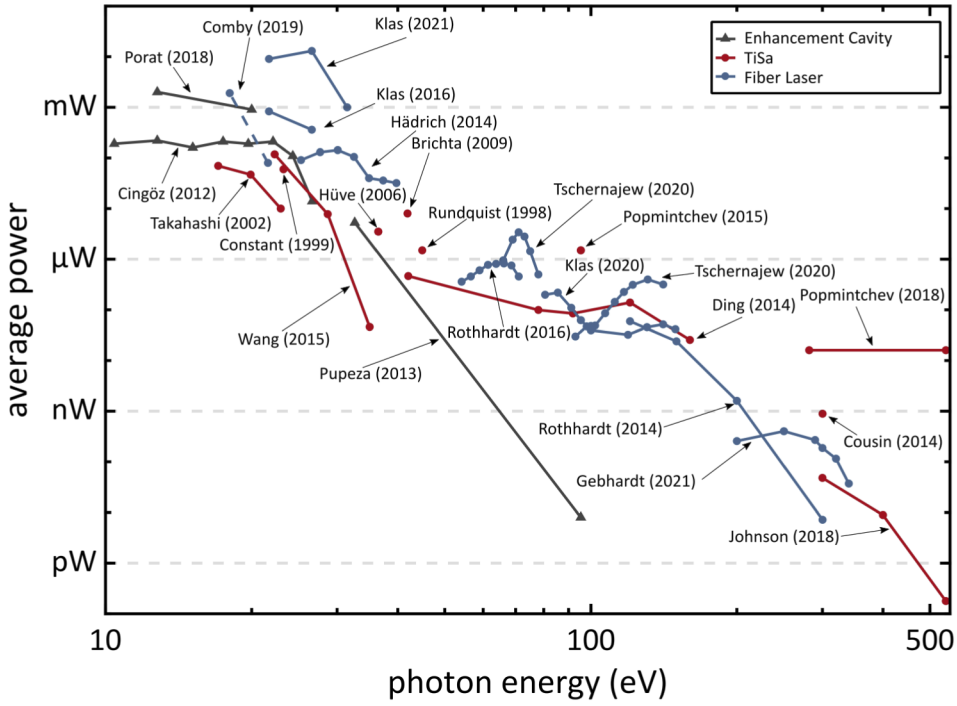

Fig. 2. Overview on the current state-of-the art high photon flux HHG sources. Single-pass HHG sources based on Ti:Sa driving lasers are shown in red, while those based on fiber laser systems are shown in blue. HHG sources based on enhancement cavities are shown in black. The data has been taken from [40,42,61–64,68–84].

Optics EXPRESS

A general trend, which is valid for all HHG sources, can be seen in Fig. 2: The average power decreases with increasing photon energy. The highest available average power per harmonic (or per bandwidth) is in the milliwatt range up to 32 eV and then drops to only 30 μW per harmonic at 40 eV. At ~ 70 eV this is further reduced to a few μW and at shorter wavelengths, the reported average powers are even lower. This has important implications for nanoscale imaging. Abbe's limit states a proportionality between the wavelength used and the achievable resolution. Thus compact XUV setups benefit from short wavelengths to achieve a high spatial resolution. At the same time, a higher resolution increases the demand for photon flux nonlinearly. Rose estimated that the photon flux required to resolve a two-dimensional object at a fixed contrast level scales inversely with the square of the required resolution [85]. For three-dimensional imaging applications, where the contrast level depends on thickness, the required flux has been estimated to scale even with the inverse fourth power of the required resolution [86]. A compromise between a sufficient average power and a preferably short wavelength has to be found. Thus, current table-top ptychography setups operate at wavelengths between 40 nm and 13.5 nm.

2.2. Coherence

An important advantage of HHG sources for lensless imaging applications is their high degree of spatial coherence, which they inherit by phase-coupling to the driving laser. Systematic measurements of the degree of spatial coherence have been performed at various harmonic sources via double-slits [6,8,87,88] or non-redundant pinhole arrays [89]. Fringe visibilities larger than 90 % have been reported for optimized generation conditions and small slit (pinhole) separations, as shown in Fig. 3(a) (reproduced from [8]). Intensity-dependent phase distortions can nevertheless alter the degree of spatial coherence of high harmonics. Thus, HHG sources generally have to be treated as partially spatially coherent. By optimizing the generation conditions and selecting the central part of the harmonic beam, a high degree of spatial coherence can be achieved. More details on the underlying physics may be found in [90] (in the context of HHG) and in [91] (for more general reference).

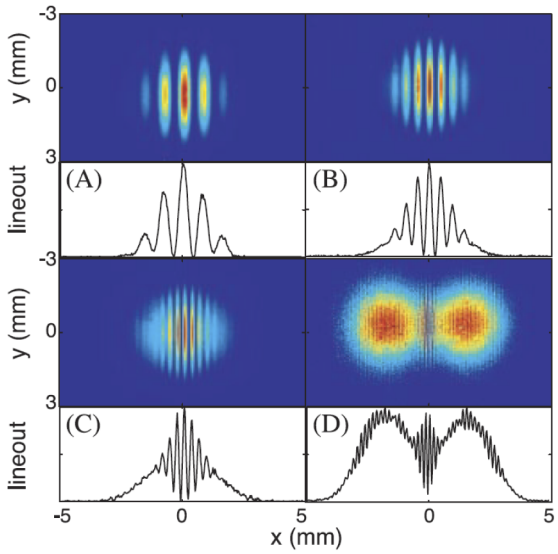

Fig. 3. Diffraction pattern of a high harmonic beam (~ 5 harmonics centered at 31 eV) behind pinhole pairs of various separations, together with lineouts of the images. The separations are (a) 142 μm, (b) 242 μm, (c) 384 μm, and (d) 779 μm. Reproduced from [8] / reprinted with permission from AAAS.

Optics EXPRESS

2.3. Pulse duration and spectral characteristics

The process of HHG occurs within a very short temporal window, usually in <10 % of the oscillation period of the driving laser [60]. For multi-cycle driving pulses, the process is repeated at every half-cycle of the driving laser with sufficient intensity resulting in a burst of attosecond pulses in the time domain and odd multiples of the fundamental frequency in the spectral domain. If the harmonic emission is restricted to a single half cycle, isolated attosecond pulses can be generated resulting in a broad, continuous spectrum. Both isolated and bursts of attosecond pulses are well suited to probe ultrafast dynamics [2]. However, their broad bandwidth hinders a direct application to lensless imaging and, in particular, ptychography. Thus, only a small fraction of the broad harmonic spectrum is usually selected and focused on the sample. Recent developments aim at enabling lensless microscopy with the very broad bandwidth of attosecond pulses, which will potentially enable material-specific, three-dimensional and ultrafast imaging. The related techniques and opportunities will be discussed in section 5.

2.4. Interaction of extreme ultraviolet light with matter

In the XUV as well as in the x-ray spectral region, the optical response is dominated by prominent absorption edges. These edges appear as a result of ionization of core electrons into an unbound state when the photon energy is sufficiently high. The shell from which the electron is excited determines the name of these edges to K-, L-, M-, N-, O- and P- edges. As shown in Fig. 4, nearly all elements of the periodic table exhibit at least one characteristic absorption edge in the XUV spectral region. At energies slightly above these characteristic edges the absorption coefficient is usually high, which can be exploited for high contrast imaging. In addition, the refractive index experiences a strong modulation in the vicinity of absorption edges, which can lead to a significant phase shift of transmitted XUV light. Despite the numerous absorption edges and typically short penetration depths, there are a few spectral regions, where some materials are rather transparent, often referred to as *transparency windows*. In the XUV, Na, Mg, Cs, Al, Rb, Si, Sr and Zr provide suitable spectral windows with absorption lengths >0.5 µm. In the soft x-ray region, C, Ca, Sc, Ti, and water provide suitable windows for imaging at finite penetration depth. The most relevant transparency windows are displayed as horizontal bars in Fig. 4. The so-called water window has been included in this graph, since it is a well-known spectral region for biological imaging. Here water provides absorption lengths up to 10 µm, while carbon is highly absorbing. This has already enabled 3D tomography of whole biological cells at a synchrotron beamline [92].

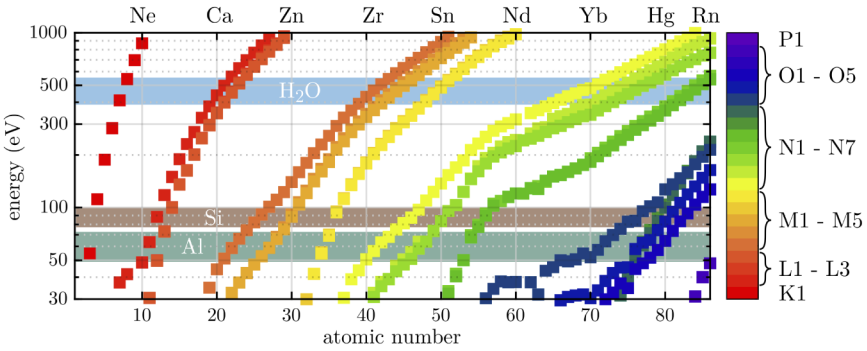

Fig. 4. Overview on the characteristic absorption edges in the XUV and soft x-ray spectral region for elements with an atomic number up to Z=86. The color encodes the shell from which the electron is excited. The green, brown and blue horizontal bars mark the transparency windows of aluminum, silicon and water. Data taken from [93].

Optics EXPRESS

The diversity of absorption edges allows high contrast imaging in transmission with reasonable penetration depth in many cases. However, the material composition of a sample has to be taken into account in order to identify a suitable photon energy for imaging. In reflection, amplitude and phase are also strongly dependent on the wavelength. Figure 5 illustrates the dependency of the optical properties of various materials on the angle of incidence and the energy of the incoming XUV beam (data from [93]). Figure 5(a) depicts the reflected intensity of the s-polarization component of the incoming beam for selected elements as the angle between the optical axis and the sample surface normal is varied. In this convention, 90 degrees corresponds to grazing incidence. The different refractive indices for the various components give rise to characteristic element-specific curves. This effect has recently been exploited to distinguish different materials in an angle-resolved, reflection-mode ptychography setup [94]. In Fig. 5(b), the reflected intensity for the s-polarization component of the incident field is shown for a fixed angle of 70 degrees (20 degrees from grazing incidence). Here, for example the magnetic transition metals (Fe, Co, Ni) show characteristic M-edge signatures in amplitude and phase within the 52 eV to 68 eV range, followed by the Al L-edge at 73 eV. Figure 5(c) shows the transmission of various elements assuming normal incidence and a layer thickness of 50 nm. Again, the characteristic absorption edges are clearly visible in amplitude and phase. Both in reflection and transmission energy-resolved imaging thus promises element specificity if the wavelength range is correctly chosen. While energy-resolved ptychography has not been used for element specificity in table-top XUV microscopy to date, recent studies indicate that this is a nearby technology [95,96]. Generally, the transmissivity of all elements increases towards higher energies and the reflectivity decreases. Current tabletop ptychography setups deploy energies below 100 eV for which reflection geometries tend to provide a higher flux on the detector than in transmission. While this is true for most but not all elements, reflection geometries additionally avoid the need for elaborate sample thinning and are therefore particularly advantageous. Overall, the XUV spectral region offers many opportunities for element-specific imaging both in reflection and transmission.

2.5. Pixelated detectors for the extreme ultraviolet

Charge-coupled devices (CCDs) have been the detector of choice for many scientific imaging applications during the last decades [97]. Commercially available back-illuminated CCD cameras enable efficient direct detection of XUV photons in vacuum with a high quantum efficiency and 100 % fill factor [98]. In addition, cooling of the detector via multi-stage Peltier-elements reduces thermal noise to a minimum (<0.001 e-/pixel/s). However, applications in ptychography suffer from a severe readout speed limitation due to the charge transfer from pixel to pixel. Typically, the readout of a single 4 megapixel image requires >4 s at 1 MHz readout rate. Although faster readout rates are possible, they are typically not used for XUV ptychography in order to avoid an increase in electronic noise. Recently, a new generation of back-illuminated scientific complementary metal–oxide–semiconductor (sCMOS) cameras has been developed for applications in the XUV and soft x-ray spectral region [99,100] and first devices are becoming commercially available [101,102]. The sCMOS architecture allows for enormous frame rates up to 74 Hz for 4 megapixel images, which is more than two orders of magnitude faster as compared to XUV CCDs. In addition, sCMOS detectors provide superior quantum efficiency and linearity. However, compared to XUV CCDs the pixel well depth is lower and the dark current is nearly two orders of magnitude higher. Table 1 summarizes the most important technical parameters of typical XUV-CCD and XUV-sCMOS detectors. Depending on the application, the most suited detector can be selected. If a low dark current is required (e.g. at integration times >10 s), CCDs are the best choice, while high frame rates and thus high scanning speeds can be achieved with sCMOS detectors.

Optics EXPRESS

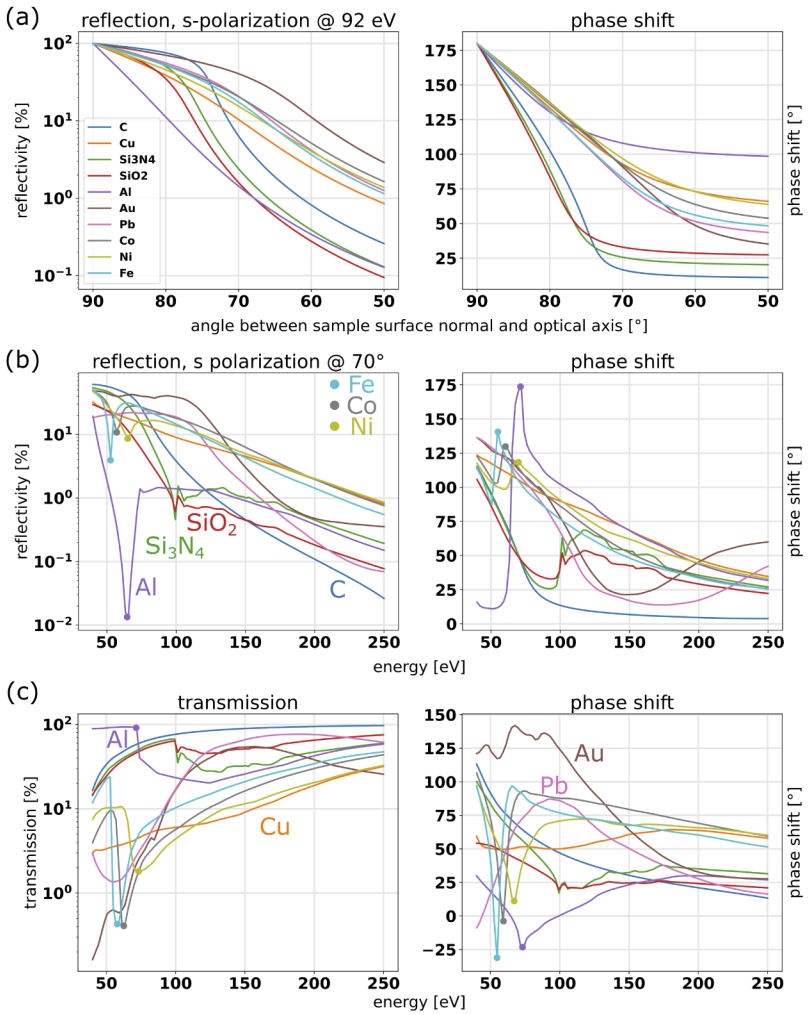

Fig. 5. Reflectivity and transmissivity of various materials. (a) Reflectivity versus angle of incidence for s-polarization at 92 eV, (b) reflectivity versus photon energy for s-polarization at 70 degree angle of incidence, (c) transmissivity versus photon energy. The transmission plots in (c) assume a layer thickness of 50 nm.

In the future, cryogenically-cooled detectors may offer additional capabilities such as noiseless detection of single XUV photons. Moreover, their energy resolution can be of the order of 2 eV, which would allow to determine the energy of each detected photon [103]. This would ultimately enable spectrally-resolved imaging, when combined with a broadband illumination from HHG sources.

Optics EXPRESS

Table 1. Key parameters of typical pixelated XUV detectors. Abbreviations: quantum efficiency (QE), no information available (n/a). Units:

Camera type	Andor iKon-L [98]	Andor Marana-X [101]	Sydor Wraith [102]
sensor	CCD	sCMOS	sCMOS
frame rate	0.2 fps	44-74 fps	24-48 fps
pixels	2048x2048	2048x2048	2048x2048
pixel Size	13.5 µm	6.5 µm	11 µm
readout-noise	7.0 e-	1.6 e-	1.6 e- / 2.6 e-
dark current[a]	0.0004 @ −80°C	0.1 @−45°C	0.5
pixel well depth	150000 e-	55000 e-	80000 e-
QE (@13.5 nm)	>85 %	>95 %	n/a
fill factor	100 %	100 %	n/a
linearity	>99 %	>99.7 %	n/a

[a]e-/pixel/s.

3. XUV tabletop ptychography

3.1. CDI and STM

Before discussing XUV ptychography, we revisit the principles of its predecessors, namely coherent diffraction imaging (CDI) and scanning transmission microscopy (STM). Both techniques are illustrated in Fig. 6 as they typically appear in a XUV tabletop experimental setup. Here we assume the driving laser is upconverted via HHG to a polychromatic XUV beam. The XUV beam is separated from the infrared (IR) driving laser by means of suitable filter membrane or grazing incidence plates (not shown here) [104]. The remaining polychromatic XUV beam is subsequently spectrally filtered to a single harmonic by means of a single or a cascade of multilayer mirrors. At this stage, the setup geometries of CDI and STM differ from each other. In CDI, a plane or weakly divergent wavefront illuminates the sample. The resulting diffraction pattern is recorded on a pixelated detector, for instance a CCD or CMOS. The imaging task is formulated as an inverse problem, typically solved by iterative optimization algorithms, as described in more detail below. In STM, the sample is sequentially scanned through a focused spot. Lateral movement of the sample allows a pixelwise information acquisition. In principle, only a single-pixel detector such as a photo diode is needed, which records information about the local transmissivity of the sample. The collected data is then rearranged into a two-dimensional image.

We start with a more detailed description of CDI. We restrict this discussion to Fraunhofer diffraction. For completeness we mention that highly curved and spatially extended wavefronts have been used in CDI, which often result in an observation adequately approximated by Fresnel diffraction [105–107]. In the Fraunhofer regime, the exit wave undergoes a spatial Fourier transformation as it propagates from the sample exit plane to the observation plane, where a pixelated detector records the intensity of the diffracted electric field. By lack of phase information, the measured intensity cannot directly be back-propagated to form an image of the sample. Alternative techniques such as holography [108] use an external reference superimposed upon the diffracted wave, encoding the specimen's phase information into the recorded interference pattern. *A priori* knowledge of the reference wave enables unambiguous and deterministic recovery of the sample phase information. However, generating a high quality external reference beam in a typical XUV tabletop setup is highly non-trivial, since the illumination suffers from aberrations induced by all optics upstream of the specimen. In addition, wavefront splitting as well as recombination optics downstream of the sample, each introducing

Optics EXPRESS

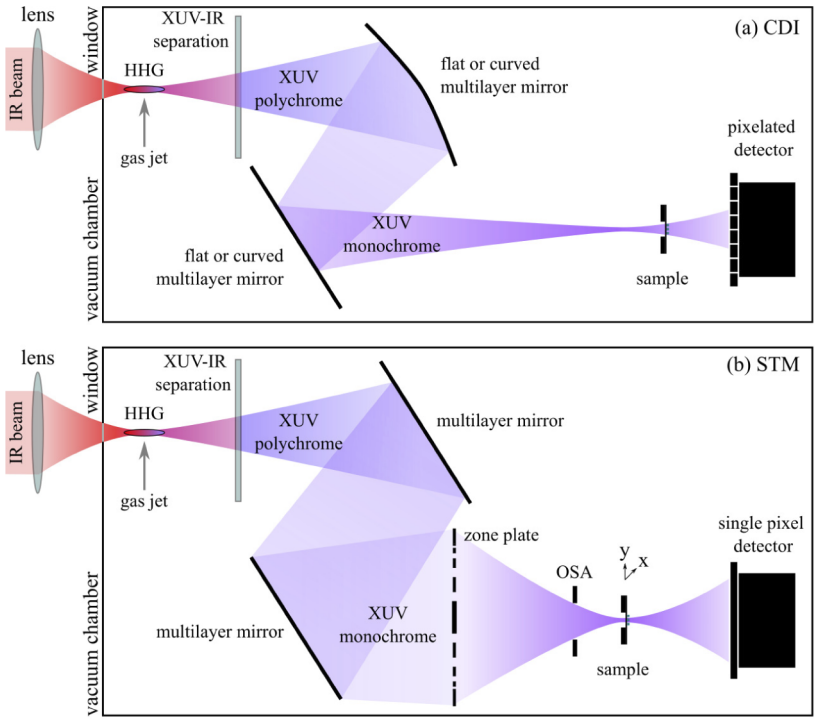

Fig. 6. Comparison of CDI and STM experimental configurations: (a) In CDI a sample is illuminated with a plane or weakly curved illumination to produce a far field diffraction pattern on a pixelated detector. (b) In STM a sample is raster scanned through a strongly focused beam. In principle, only a single-pixel detector is needed to measure a transmission image of the sample. An order sorting aperture (OSA) is required to block the undiffracted signal contributions from the Fresnel zone plate.

additional absorptive losses and aberrations, would be required. In Fourier transform holography (FTH) [109–111] this problem is bypassed by placing a small pinhole in the vicinity of the sample of interest, generating a high-quality reference wave. However, FTH requires elaborate nanofabrication techniques, which may not be suitable for some wide field of view or biological samples. Unlike FTH, CDI takes a reference-free approach to solve the phase problem. Here the sample is confined in lateral extent, which is also referred to as a *finite support*. Because the sample and observation plane are Fourier conjugates, a sufficiently small sample size renders the detector signal effectively bandlimited, typically referred to as *oversampled* in the CDI literature [112]. The idea of oversampling dates back to the 1950s, when Sayre conjectured that direct crystallographic structure determination is possible from oversampling x-ray diffraction data. The argument was that oversampling would enable to trace zero crossings in the diffraction data, effectively determining sign changes, the most basic form of phase information and sufficient in the presence of other symmetry constraints in certain crystallographic problems. In the 1970s, Fienup proposed a class of iterative phase retrieval algorithms, which recover phase information in the presence of positivity constraints [113]. While positivity is not applicable to general, complex-valued waves, it can be used in synthetic aperture radar (SAR). In SAR the Van Cittert-Zernike theorem establishes a Fourier transform relationship between an incoherent source intensity, for which positivity applies, and its far-field degree of spatial coherence [91]. A recent prominent example is the Event-Horizon-Telescope, which produced the first image of a black hole by virtue of SAR [114]. In the 1980s, Fienup also observed that a Fourier

Optics EXPRESS

diffraction intensity in conjunction with *strong* knowledge of the finite support of a sample suffice to reconstruct complex-valued specimens, replacing positivity in earlier work. The word "strong" here refers to the early observation that *a priori* available knowledge about the support has to be precise in terms of size and shape and that certain topologies (e.g. separated, non-overlapping ellipses) work better than others (for instance non-convex but contiguous supports) [115]. Almost half a century after Sayre's proposal and a decade after Fienup's work, Miao et al. successfully demonstrated the first x-ray CDI experiment at a synchrotron source [22]. This new technique rapidly gained momentum in the synchrotron and free-electron laser (FEL) communities. At synchrotrons CDI has been used for biological and three dimensional imaging [92,116]. At FELs it found application in so called "diffract-and-destroy" single particle imaging, where femtosecond x-ray pulses diffract from a crystalline structure before radiation damage sets in [117,118]. Progress in algorithm development enabled iterative estimation of a tight support [26] (compare Fig. 7) as well as the correct alignment of randomly oriented single particles [119] along with the phase of the diffracted wave - both important results for experimental practice, where strong support and orientation knowledge is otherwise hard to come by.

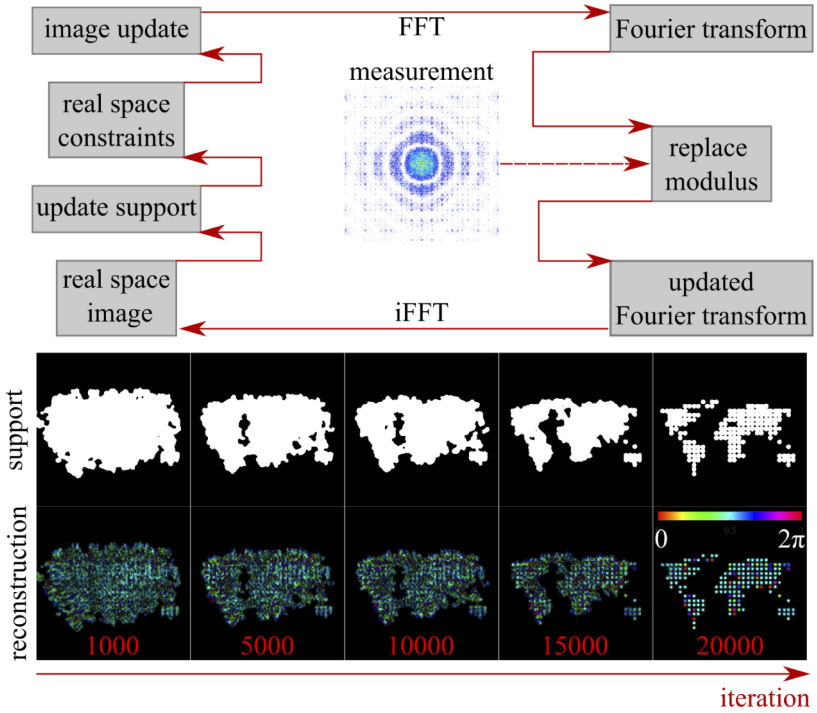

Fig. 7. Typical algorithmic workflow in CDI as described in [26]. An initial estimate for the object is propagated into the detector plane (FFT: fast Fourier transform). There its modulus is replaced by the measured data. The updated Fourier estimate is backpropagated into the sample plane (iFFT: inverse fast Fourier transform). From the updated real space estimate, an improved support can be extracted. A finite support constraint, together with potentially other a priori knowledge of the sample, if enforced to get an improved real space estimate of the sample. The algorithm iterates until no further progress is made, as judged by the difference between the Fourier estimate and the measured data. The colormap encodes modulus and phase of the reconstructed field as brightness and hue, respectively. An example shrink wrap code is publicly available at [120].

The advances in the synchrotron community were paralleled by constant improvements in the available flux from tabletop HHG sources. In 2007, Sandberg et al. reported the first CDI

Optics EXPRESS

experiment with a tabletop HHG source [23]. In the XUV range, the lensless operation mode of CDI was a much needed addition to existing techniques in order to avoid the aforementioned disadvantages of lens-based full field microscopes. However, the low penetration depth of XUV as compared to x-rays restricted the application of CDI to thin samples. An important step forward in CDI was its generalization to reflection geometries, where the sample and observation plane are non-coplanar [121]. Towards grazing incidence, i.e. an angle between the sample surface normal and the optical axis close to 90°. High numerical aperture (NA) correction strategies were reported that allowed CDI to approach wavelength-scale lateral resolution at XUV wavelengths [122–124]. Combinations of CDI with Fourier transform spectroscopy have been reported, that principally open up spectral tuning [125] and wavelength-resolved imaging [126,127]. Combinations of CDI and shearing interferometry have been developed, which coherently superimpose a differentially shifted version of the detector wave with itself, thereby directly encoding the phase gradient [128,129]. We note that both spatial and temporal coherence requirements in CDI have been investigated [130,131]. More information is found in several excellent reviews covering CDI and its underlying algorithmic techniques [24,25,27,28,132–135].

We now turn to a brief overview of STM, where we restrict our discussion mainly to the short-wavelength regime. In 1951, Young and Roberts proposed the first optical scanning microcsope to avoid loss of light and aberrations associated with imperfect lenses [136]. Two years later Pattee theoretically described a STM configuration using a microfocus x-ray tube [137]. In 1956, two articles appeared side by side in the same issue of the journal Nature, reporting STM with ultraviolet [138] and hard x-ray [139] radiation. The first STM at a synchrotron source was reported in 1972 by Horowitz and Howell [140], who used a 2 μm pinhole to create a x-ray scanning probe. However, the lateral resolution in STMs is limited by the size of the illuminating beam [141,142]. An important step towards smaller spot sizes was made in 1984 by Rarback et al., who demagnified a 30 μm aperture by means of a Fresnel zone plate (ZP) into a 300 nm focal spot [143,144]. This experimental geometry has subsequently been refined to achieve a lateral resolution of 25 nm in a highly focused synchrotron beam [145]. Chapman demonstrated a Wigner distribution deconvolution (WDD) on x-ray STM data as early as 1996 [146]. While WDD techniques are memory consumptive and in the form reported by Chapman require *a priori* knowledge of the focal spot, they are an important precursor to later memory efficient ptychographic deconvolution algorithms and remain important from a theoretical perspective [10]. Apart from the synchrotron community, the first tabletop XUV scanning microscope was demonstrated in 1989 by Trail and Byer [12], who reported a laser-produced plasma source focused by means of a Schwartzschild objective to achieve a spot size of 500 nm. An HHG-based scanning microscope was developed by Früke et al. with a resolution better than 1 μm [14].

Similar to CDI, STM is a lensless technique, since no imaging optics are used. Nevertheless, CDI and STM perform rather differently in terms of resolution, speed, and multimodality. Considering lateral resolution, illumination optics are typically employed in STM to produce a small focal spot, while in CDI the illumination wavefront is expanded and at most weakly curved. In contrast to CDI, STM requires only a single-pixel detector, although extensions to segmented detectors have been demonstrated and open up the possibility of differential phase contrast imaging [141,142,147]. In the theoretical limit of an infinitely small detection numerical aperture (NA_d), STM produces a scanning micrograph at the resolution of the spot size produced by the illumination optics. On the other hand, in CDI a perfectly coherent plane wave illumination, which by definition corresponds to a negligible illumination numerical aperture (NA_i), can produce a reconstructed image with a resolution only limited by the detection numerical aperture - provided appreciable photon flux is recorded at the highest diffraction angles accessible by the detector. Summarizing, the lateral resolution in STM is primarily limited by the illumination NA, while in CDI the detection NA is the key factor. While the illumination NA can experimentally be controlled, signal at high detection angles in CDI is only observed for strongly scattering

Optics EXPRESS

specimens. Thus, arguably STM has the advantage over CDI that it delivers a high lateral resolution independent of the particular specimen choice.

Another consideration is speed. While visible light STMs typically operate with galvo mirrors, which rapidly steer a focused beam over a sample of interest, it is more challenging to obtain a uniform spot in x-ray STMs using beam steering [148]. X-ray STMs require an order-sorting aperture (OSA), which blocks unwanted diffraction orders from the ZP. The combination of ZP and OSA would result in a highly position-dependent focal spot, if one attempted to illuminate the ZP with angularly varying plane waves. It is therefore preferred to have a stationary focal spot and scan the sample by means of a high-resolution translation stage. Thus CDI is principally single-shot, which justifies its use in femtosecond crystallography, while STM is inherently slow due to mechanical translation of the sample.

Finally, we consider multimodal imaging. The workhorse for chemical sensitivity in x-ray data analysis is fluorescence. In contrast to CDI and other wide field techniques, STM can be combined with fluorescence detection, thanks to the confinement of high intensities to a localized spot. In this configuration, an energy-resolved single-pixel detector is added to the experimental setup. Unlike the elastically scattered coherent radiation, which is mainly detected in the beam propagation direction, the incoherent fluorescence signal is emitted omnidirectionally, which allows its detection off-axis. Moreover, there is no need to image the fluorescence signal via optical elements, since it can be attributed to the focal spot, enabling direct localization. A wide field geometry would require imaging optics, which for hard x-rays are either highly dispersive (ZPs, compound refractive lenses) or suffer from space-variance and low acceptance angles (curved mirrors) [149]. Wide field techniques would also require pixelated, energy-resolved detectors. Although such detectors exist, they do not feature the required resolution for wide field imaging with large space-bandwidth product. Because the fluorescence yield diminishes at photon energies below the water window [150], we do not see an efficient route towards fluorescence detection in the XUV in the near-future. However, fluorescence detection could become relevant when high-flux high harmonic sources in the water window become readily available [151]. Other contrast modalities such as second harmonic generation, which has recently been experimentally demonstrated in the XUV [152] with an observed efficiency of 2%, could become a feasible route towards multimodal XUV STM.

3.2. Ptychography: algorithmic workflow and sampling considerations

In ptychography, the single-pixel detector in a STM configuration is replaced by a pixelated detector. This modification would be of no consequence if the sample would be illuminated with a point-like illumination, resulting in only one type of signal that can be sent from the sample to the detector - a spherical wave. In practice, however, the spot size is spatially extended and the variety of signals that can be sent from the sample combinatorially grows with increasing spot sizes. A single-pixel detector would simply integrate over each diffraction intensity, while a pixelated detector allows to distinguish between different signals. While using a loosely focused beam is still required to meet certain sampling requirements in ptychography (detailed below), the measured signal now also contains characteristic interferences, which are indicative of spatial frequency content present in the sample and illumination. We may invoke the analogy of a ptychographic data set to sheet music. The latter describes a piece of music by specifying frequencies played at particular time signatures, thus simultaneously providing time and frequency information. However, while a recording of a musical score can be time-frequency analyzed to fully retrieve an accurate description of the musical piece at hand, at optical frequencies the diffraction pattern lacks phase information. We thus face a similar problem as in CDI. Unlike in CDI where a priori knowledge is required, in ptychography the sample is translated such that adjacent scan positions laterally *overlap* (see Fig. 8(a)). In this way, every object position is measured multiple times, effectively overconstraining the phase problem and avoiding the need

Optics EXPRESS

for prior information, apart from the knowledge of the positions provided by the encoder of the scanning stage. Thus ptychography is often described as a *scanning version of CDI*, although it is equally true to describe it as a *diffraction-resolved version of STM*. The first statement emphasizes that in ptychography diffraction patterns are recorded which lack phase information, similar to CDI. The second statement underlines that ptychography involves sample scanning - similar to STM - with the additional ingredient of spatially overlapping positions enabling phase retrieval.

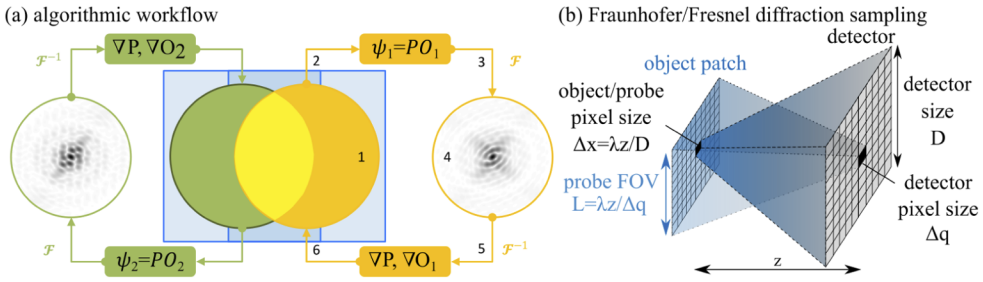

Fig. 8. (a) Algorithmic workflow in ptychography: 1) Select scan position, 2) form exit wave, 3) propagate, 4) modulus projection, 5) back-propagate, 6) apply probe and object gradients. (b) Sampling requirements in ptychography from which pixel size Δx and probe field of view L follow. Panel (b) assumes Fraunhofer or Fresnel diffraction.

Figure 8(a) shows the algorithmic principle of ptychography. We assume an STM setup (compare Fig. 6(b)) with the single-pixel detector replaced by a CCD or CMOS camera. As shown in Fig. 8(a), the sample (blue region) is translated such that illuminated regions laterally overlap. Here the green and orange circles indicate the beam's footprint on the sample, which is assumed to be larger than the beam. After randomizing the initial object and probe estimate, an iterative algorithm performs the following steps: (1) Select a scan position. (2) At the given position, form estimated exit surface (ESW) wave ψ downstream of the specimen; in Fig. 8(a) the thin element approximation is assumed, modeling the ESW as a product of incident beam P and object O. (3) Propagate ESW to detector plane. (4) Replace modulus of the estimated detector wave with the square root of the measured diffraction intensity. Keep the phase of the estimated detector wave. Step (4) is referred to as the *modulus projection*. (5) Back-propagate the updated detector wave to the sample plane. (6) Apply gradients to the local object patch (blue square) and probe (orange). Repeat steps (1) to (6). The green circle illustrates the probe of a possible choice for the second selected position. The overlap (yellow region) with the previous scan position now puts the algorithm into a better situation than what it started from: The first cycle through steps (1) to (6) has already improved the probe and sample estimate, thus enabling propagation of information between adjacent positions. Although this exchange of information between adjacent positions is non-interferometric, it enables computational phase retrieval. We note that many variations of steps (1) to (6) in the iterative optimization procedure exist, including multiple scattering models in thick specimens [153–155], modified propagators accounting for near-field effects [156] and curvature correction in high NA as well as reflection geometries [121,123,157], partial coherence [158–160], various types of self-calibration routines of the experimental setup [161–164], and accelerated gradient techniques [165–167]. A comprehensive overview of these techniques is given in [10].

Figure 8(b) shows the most typical sampling conditions encountered in XUV ptychography. We assume an experimental geometry has a Fresnel number $F = L^2/\lambda z \lesssim 1$ on the order of 1 or smaller. Here λ, z and L denote wavelength, sample-detector distance, and the numerical probe field of view, respectively. Under the aforementioned circumstances, propagation from the sample to the detector plane is described by the Fresnel or Fraunhofer diffraction integrals, which differ only by a quadratic phase factor [168]. The relevant quadratic phase factor is equal

Optics EXPRESS

for all scan positions. Therefore it can be absorbed into the reconstructed probe estimate and may be ignored unless one is interested in quantitative wavefront diagnostics. In this case, the quadratic phase has to be compensated to get quantitative estimates for the probe wavefront. For both Fresnel and Fraunhofer diffraction, the pixel size Δx in the sample plane is given by

$$\Delta x = \lambda z / D, \tag{1}$$

where D is the size of the detector. The smallest resolvable element in the sample plane is inversely proportional to the largest measurable signal distance in the detector plane - a direct consequence of the uncertainty relation for signals that form Fourier transform pairs [169]. We emphasize that the pixel size Δx is generally not equal to the lateral resolution to be expected in the final experiment. For the lateral resolution to approach the pixel size limit, also called *diffraction-limited resolution*, sufficient signal to noise at high angles in the diffraction data is required. When sufficient photon flux at high angles is available, the experimenter may decrease the wavelength and/or the sample-detector distance to improve the lower bound set by the diffraction limit. The second sampling condition is the probe field of view L given by

$$L = \lambda z / \Delta q, \tag{2}$$

where Δq is the detector pixel size (after optional binning). Here the largest distance in the object plane that can be sampled from a single diffraction pattern, the probe field of view, is inversely proportional to the smallest feature in the detector, the pixel size. In the planning stage of an XUV ptychography experiment it is important to select focusing optics that confine the beam to a size smaller than the probe field of view. In typical XUV ptychography setups the probe field of view is limited to a few up to tens of micrometers. In case that the physical probe is larger than the numerical limit set by the finite probe field of view, the diffraction data is undersampled. Although algorithms [170,171] for ptychography exist that increase the effective probe field of view by subsampling the detector pixels, undersampling should - if possible - be avoided in the planning stage of a ptychographic beamline. Subsampling increases computational overhead and requires higher overlap between scan positions in order to allow recovery of the missing subpixel information, ultimately necessitating higher data throughput and longer scan times. It is typically experimentally easier to either reduce the probe spot size or increase the sample-detector distance (at the expense of diffraction-limited resolution).

A practical consequence from Eqns. 1 and 2 for XUV ptychography is that the reconstruction pixel size scales with wavelength. While it poses no additional experimental challenges when polychromatic radiation is used, it is a particular concern for data analysis. The problem is that if the probe field of view is wavelength dependent, then addressing the object patch at each scan position is a function of wavelength, complicating the arrays that keep track of the pixels limits in each object patch. In addition, multispectral ptychography can benefit from regularization, where for instance differences in the spectral object reconstructions at neighboring wavelengths are penalized to enforce spectral continuity. Such regularization techniques are significantly easier to be implemented if the spectral object estimates reside on a sampling grid that is the same for all wavelengths involved. There are two main approaches that enable uniform grids in multispectral ptychography. (1) Zero padding the estimated detector wave before and cropping the updated exit wave after back-propagation into the sample [172]; (2) two-step propagators, which utilize an angular spectrum propagator combined with a Fresnel propagator to rescale the pixel size [96]. While the first approach comes at the price of a certain amount of pixel index bookkeeping and a slight increase in computational complexity, the second approach requires two Fourier transforms with the same number of pixels as the original probe field of view.

Optics EXPRESS

3.3. XUV Ptychography: experimental configurations and state of the art

The most common XUV ptychography experimental configurations are shown in Fig. 9. Panel (a) depicts a transmission-mode setup, where a camera is placed coplanar to and downstream of a transilluminated sample. In a transmission-mode experimental geometry far-field diffraction is modeled by a Fourier transform operation. Figure 9(b) shows a reflection-mode setup, where the sample and detector are non-coplanar. Far-field diffraction in a non-coplanar reflection-mode setup may be computed via a Fourier transform followed by an additional interpolation step in the detector plane to take into account curvature effects that arise in non-coplanar diffraction geometries [121,157]. Figure 9(c-e) show possible illumination optics for XUV ptychography. So far, reflective mirrors are the most typical choices, due to their capability to monochromatize the incoming XUV beam when multilayer coatings are present. The first XUV ptychography demonstration (see Fig. 10(a)) employed a spherical multilayer mirror in a reflection-mode geometry [11]. Shortly after, a reflection-mode ptychography experiment employing an ellipsoidal mirror was reported [173]. In a transmission-mode geometry (see Fig. 10(b)), reflective optics can be combined with a pinhole placed close to the focal plane in order to clip the tails of the focal spot. This produces a highly localized beam with additional benefits resulting from additional spatial frequencies introduced by the pinhole edges [174]. Transmission-mode XUV ptychography was first demonstrated in [175], where a combination of a single spherical multilayer mirror and a pinhole close to the focal plane was used. In reflection mode ptychography adding a pinhole close to the focal plane is no option; because the sample is tilted, there is an immediate requirement for a large working distance to any optical elements upstream. An alternative to reflective optics are diffractive focusing optics. Zone plates (ZPs) are typically used in conjunction with order-selecting apertures (OSAs), which filter the first diffraction order which is used for focusing from unwanted radiation (see Fig. 9(d)). ZPs enable high numerical aperture beam focusing at relatively large working distances; the OSA may be placed relatively far upstream of the focal plane (several millimeters for XUV radiation). In addition, zone plates may be used for holographic beam shaping to create functional beams carrying, for instance, orbital angular momentum [32], or to create structured illumination, which has been shown to significantly improve reconstruction quality in ptychography [174,176–179]. The first XUV ptychography experiment employing a zone plate for beam structuring was demonstrated in [96], where wavefront sensing on a multispectral beam was reported (see Fig. 11). While amplitude-modulating transmissive ZPs are limited to approximately 10% efficiency, reflective phase-modulating ZPs could principally reach higher diffraction efficiencies. However such reflective ZPs are considerably more complicated to fabricate, as they require larger aspect ratios and curvature corrections when used in non-coplanar focusing geometries. Other illumination optics such as Schwartzschild objectives may find applications in XUV ptychography in the future. The latter are interesting candidates as they reach high numerical aperture and exhibit an annular diffraction cone, which could mitigate dynamic range limitations in recording diffraction patterns that are strongly peaked in the on-axis or specular direction.

A few practical considerations are worth being addressed here. As seen from Fig. 5, the XUV spectral range offers the chance for element-specific microscopy. Transmission- or reflection-mode ptychography may be used to measure both amplitude and phase change upon transmission/reflection. A first step into this direction was done by Zhang et al., who reported a multispectral reflection-mode ptychography experiment with 4 harmonics present in the illumination [95], resulting in a scan of polychromatic diffraction patterns recorded on a monochromatic camera. The challenges in disentangling incoherent signal mixtures added up on a detector are surmounted by the large amount of data available in ptychography, afforded through oversampling and overlap. Both partial spatial coherence [158] and multiple colors in the illumination [159] may be solved for. This is particularly relevant for XUV ptychography, since scanning the photon energy and carrying out separate monochromatic scans is both

Optics EXPRESS

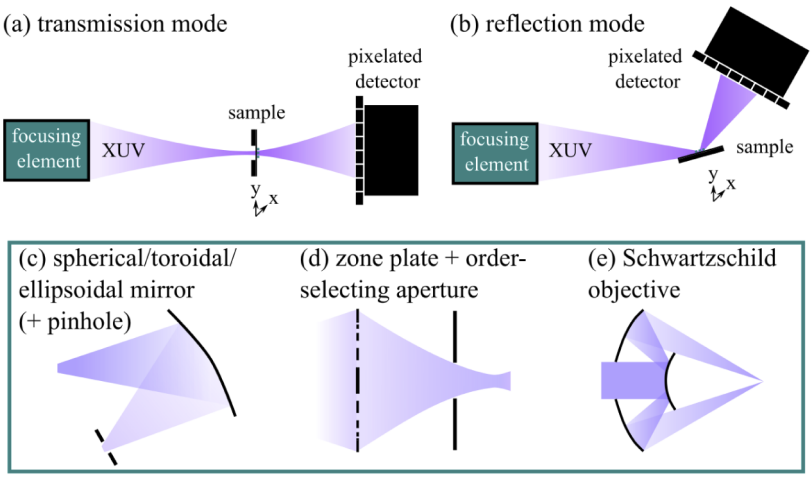

Fig. 9. Typical operation modes in ptychography: (a) transmission and (b) reflection. A variety of reflective and diffractive optics may be used to focus radiation onto the specimen: (c) spherical, toroidal, or ellipsoidal mirror with optional pinhole, (d) zone plate and order-selecting aperture, (e) Schwartzschild objective.

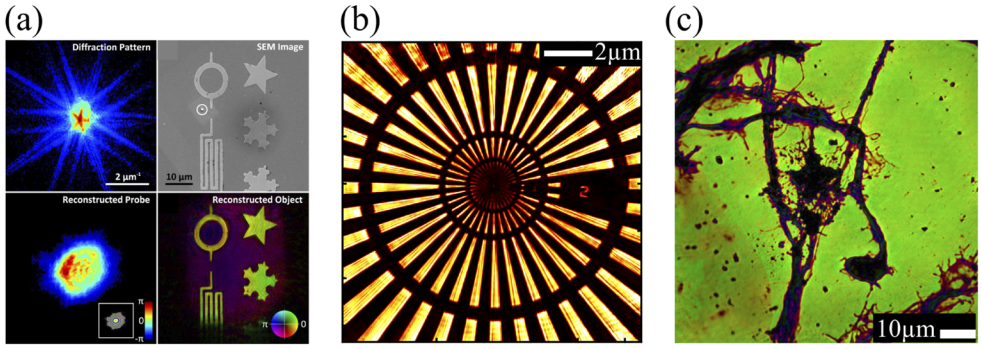

Fig. 10. Experimental demonstrations of microscopy and wavefront sensing via XUV ptychography. (a) Reflection-mode (45° angle of incidence, 29 nm wavelength; reproduced from [11] with permission from OSA), (b) transmission-mode (18 nm wavelength; reproduced from [180], used under CC BY 4.0 / with modifications of the depicted field of view), (c) XUV bio-imaging of hippocampal mouse neurons (29 nm wavelength; reproduced from [181], used under CC BY 4.0 / we annotated the scale bar).

technologically challenging and time-consuming. However, comparing the multispectral results reported by Zhang et al. [95] to the monochromatic results reported by the same group on the same specimen a year earlier [173], one could easily draw the conclusion that multispectral ptychography is not robust and leads to reconstruction artefacts. However, the multispectral XUV ptychography measurements reported in [95] were performed using a relatively smooth beam, generated from an ellipsoidal mirror. For multispectral ptychography to work robustly, it is highly beneficial to use a structured illumination profile. For instance, the visible light experiments in the supplementary information in [96] separated 7 simultaneously measured spectral contributions from a monochromatic detector. In particular, a direct comparison of structured and smooth illumination profiles showed clear improvements in spectral reconstructions for the structured beams [96]. It is thus of critical importance to explore multispectral beam shaping concepts to

Optics EXPRESS

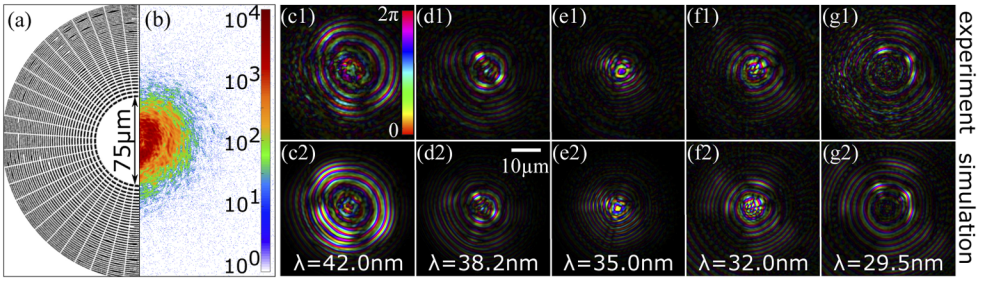

Fig. 11. Ptychographic wavefront sensing on a multispectral structured beam. (a) SEM of zone plate for XUV beam shaping, (b) 1 out of 252 diffraction patterns in the ptychography scan (scale bar shows AD counts on a logartihmic scale), (c-g) top row: ptychographic reconstruction, bottom row: simulation from known ZP profile. Only 5 our of a total of 9 reconstructed spectral wavefronts that are shown. Reproduced from Fig. 4 and Fig. 5 from [96] under OSA Open Access Publishing Agreement / we rearranged the panels.

unlock the currently unused potential of multispectral XUV ptychography for chemical sensitivity. The second route towards element specificity is to perform multiple ptychography scans, where the specimen tilt against the optical axis is varied while the photon energy is fixed. Because the specular direction changes proportionally to the angle of incidence, such an experimental setup requires additional rotation stages for sample and detector. An angle-resolved reflection-mode ptychography experiment has recently been reported by Tanksalvala et al. [94].

Before proceeding, we shortly summarize the capabilities of ptychography as compared to its predecessors STM and CDI. As shown in Table 2, ptychography has unique advantages over both STM and CDI. As compared to CDI, ptychography allows to access amplitude and phase contrast without the need for a priori knowledge and at theoretically unlimited object field of view. These advantages come at the cost of speed. While single-shot ptychography variants have been proposed, they sacrifice lateral resolution as the detector is segmented into smaller tiles, decreasing the detection NA [182]. Thus CDI (and its close relative FTH) are typically chosen when speed is critical and lensless imaging is the only option. As compared to STM, ptychography decouples the lateral resolution from the illumination spot size. Although ptychography still requires an illumination that is localized within the probe field of view (compare Eq. (2)), the lateral resolution can be orders of magnitude smaller than the spot size [32]. This is achieved via illumination wavefront sensing and its deconvolution from the object, which is a unique advantage of ptychography over CDI/STM and the key to unlock quantitative amplitude and phase information. A critical and arguably not fully understood topic is the resolution limit that may be achieved by ptychography. While the pixel size is mainly determined by the size of the detector, a highly structured illumination can be used to exceed the diffraction limit set by the detection NA [183]. However, this so-called *superresolution ptychography* requires a structured beam with high spatial frequency content, which is challenging to generate for XUV wavelengths. For strongly scattering specimens a wavelength-scale lateral resolution can be achieved with current XUV ptychography systems [173,180,181,184]. However, strongly scattering samples typically yield detectable signals at high detection angles before the detector dynamic range limit is reached. For samples that scatter mainly in the forward or specular direction, the detector dynamic range is a limiting factor: the central pixels are typically overexposed before appreciable flux at high angles can be recorded. At synchrotron beamlines, high NA illumination optics (zone plates, Kirckpatrick-Baez, and compound refractive lenses [185,186]) are typically used such that the 0-th order forward scattering cone is distributed over many pixels. At XUV wavelengths similar high-NA illumination optics are currently missing, underlining once more the need for the development of novel XUV wavefront focusing and structuring concepts.

Optics EXPRESS

Table 2. Comparison of key attributes and performance measures of CDI, STM, and ptychography. QPI: quantitative phase imaging;

	CDI	STM	ptychography
illumination	extended/plane wave	tightly focused	loosely focused
detector	pixelated	single-pixel	pixelated
speed	single-shot	scanning	scanning
QPI	limited[b]	limited[c]	amplitude + phase contrast
a priori knowledge	required	not required	not required
wavefront sensing	not possible	not possible	probe recovery
resolution[a]	λ/NA_d	spot size	data-driven
object field of view	limited	unlimited	unlimited

[a]full period lateral resolution;
[b]dependent on amount of a priori knowledge;
[b]possible with segmented detector [187], but beam contribution is not separated from object.

4. Applications

4.1. XUV wavefront sensing

While ptychography was conceived as an imaging technique, its ability to simultaneously retrieve the complex electric field of the probe beam [34,188,189] provides additional opportunities for wavefront sensing as well. In fact, comparing the achievable transverse resolution and phase sensitivity, ptychographic wavefront sensing turns out to be a competitive approach for characterizing XUV beams. The main lensless approaches to wavefront sensing, as applied to XUV beam characterization, are Hartmann sensors [190], point diffraction interferometry [191,192], lateral shearing interferometry [193], and point-scanning methods [194]. A Hartmann mask contains a regular array of apertures, which is placed in front of an image sensor. The recorded spot pattern can be compared to a reference grid, providing information on the local wavefront tilt. Hartmann sensors gained popularity as a straightforward measurement method with a fast and direct reconstruction technique, but the finite distance between apertures limits both the transverse resolution and the maximum detectable phase gradient. Thus Hartmann sensors are typically applicable on expanded wavefronts only, although variations have been reported that allow using them for focused XUV beams in conjunction with phase retrieval [195]. A higher transverse resolution may be obtained through interferometric methods: point-diffraction interferometry is largely analogous to Fourier-transform holography as used in XUV imaging, while lateral shearing is a form of self-referenced holography too. In such methods, the ability to discern fringe patterns determines the maximum detectable phase tilt, while accuracy is mainly determined by the reference beam. Some of these methods, in particular point-scanning and Hartmann masks, have been adapted to enable wavelength-resolved wavefront sensing of broadband HHG sources [194,196].

As the probe field reconstruction in ptychography has the same resolution and phase accuracy as the object reconstruction, a ptychography-based wavefront sensor (WFS) can achieve state-of-the-art performance and beyond for characterizing x-ray and XUV [30–32,34,197,198] as well as visible-light [188,199] and near-infrared beams [33]. Such a WFS basically consists of a ptychographic scanning setup, but includes an object structure that is optimized to provide strong high-angle diffraction over a large area, to ensure optimal use of the available detection NA and field-of-view. In addition, the object structure may be assumed known, to improve algorithm convergence especially in the first iterations and reduce the required amount of data that needs to be measured. To satisfy oversampling, either the beam itself should be localized as is commonly the case in ptychographic imaging, or the object can be chosen as a limited-aperture scatterer

Optics EXPRESS

to enable wavefront sensing of extended beams. Moreover, the simplest forward model in ptychography assumes that the wavefront is stable throughout the entire scan, although techniques have been reported that relax the stability assumption [198].

A major application of wavefront sensing is the characterisation of aberrations in near-diffraction-limited focusing, aiming to express a wavefront in terms of lower-order Zernike polynomials. At XUV wavelengths, this has been shown to be feasible through ptychography even when considerable pointing instabilities are present in the beam [198]. However, ptychographic wavefront sensing enables more advanced applications, such as the characterization of strongly focused and/or highly structured beams [31,32,176–178], as well as of partially spatially coherent and multi-wavelength beams through a mixed state decomposition of the probe beam [158,159]. As all HHG beams are multi-wavelength in nature, ptychographic wavefront sensing provides a powerful characterization tool for such complex beams. Quantitatively accurate wavefront sensing of complex focused beams enables the characterization of diffractive optical elements, such as Fresnel zone plates and various beam-shaping devices for XUV and soft-X-ray radiation [32,96]. An example of such ptychographic wavefront sensing of multi-spectral complex beams is shown in Fig. 11: here, a HHG beam is focused using a zone plate with additional features, and subsequently characterized using ptychography. The resulting highly structured wavefronts for all individual harmonics could be retrieved at ~ 250 nm full-pitch spatial resolution, close to the detection NA limit [96].

4.2. Ultrashort pulse characterization

The algorithmic concept of ptychography can be extended to other scanning-probe-type measurement schemes that require subsequent phase retrieval. The characterization of ultrashort light pulses is such an application area where iterative phase retrieval has become a standard approach, and recent work has led to the development of time-domain ptychography for pulse characterization [200,201]. For one of the most widespread ultrashort pulse characterization methods, known as frequency-resolved optical gating (FROG) [202], the measurement geometry is in fact almost identical. Ptychographic reconstructions can be performed on FROG datasets with superior performance [203], also enabling the ptychographic approach to dealing with partial coherence [204]. A major advantage of time-domain ptychography over projection-based FROG retrieval algorithms is the significantly smaller number of measurements needed. This data reduction ability results from the difference in resolution limits: in ptychography, the achievable time resolution only comes from the frequency space sampling, while in projection algorithms the temporal scan step size is an additional limitation [200,203]. The extension to XUV pulse characterization is technically challenging, as time-domain ptychography requires a nonlinear interaction between a probe and object pulse to provide the 'probe times object'-type forward model needed for the ptychographic reconstruction. A solution is the use of 'streaking': temporally overlapping the short 'object' XUV pulse and an extended 'probe' infrared pulse in a gas jet results in ionization, in which the resulting electron kinetic energy contains an XUV-IR two-photon component that provides the required product. This approach has been used to reconstruct complex-shaped XUV pulses, even down to the attosecond range [205–207].

4.3. Application perspective of ptychography

High-resolution imaging is an important diagnostic technique in almost every area of science. Ptychographic imaging methods using XUV radiation are also finding their way towards applications, with various proof-of-concept experiments already demonstrating its promise. The two main strengths of XUV imaging are the potential for high spatial resolution, and the ability to obtain element-specific contrast. In addition, the penetration depth into many materials can be on the order of several hundred nanometers (depending on the exact photon energy), which enables inspection of thin samples in transmission, as well as sub-surface probing of thicker structures

Optics EXPRESS

in reflection. When comparing HHG-based imaging to electron microscopy, it is actually the combination of all these aspects that makes HHG-based imaging more attractive for certain use cases, rather than a comparison based on spatial resolution alone.

Ptychography with HHG sources has been used to characterize lithographic nanostructures on EUV lithography masks, in a so-called actinic inspection configuration [208]. The authors use 13.5 nm wavelength radiation, spectrally filtered from a HHG source, in a reflection ptychography configuration at 6° incident angle. As this configuration is identical to how such a mask is illuminated in a lithography scanner, it allows quantitative characterization of amplitude and phase defects. The ability to image mask structures in phase and amplitude and to detect nanoscale defects is shown to be feasible, although the challenge remains to meet the stringent speed requirements of the semiconductor industry. We note that similar efforts are underway at synchrotron facilities, with encouraging results [209,210]. High-resolution imaging of lithographic nanostructures with chemical sensitivity was recently achieved by analyzing absolute reflectivities compared to model stack calculations [211], and further advanced through ptychographic measurements over a range of incident angles [94]. Furthermore, dynamic imaging of nanoscale surface acoustic waves was reported, through ptychographic imaging with XUV pulses preceded by an infrared pump pulse at a set time delay [212]. Physical chemistry is another field where high-resolution imaging with element-sensitivity may have significant impact, as recent work on ptychographic imaging of colloidal crystals demonstrates [213]. Ptychographic imaging and wavefront sensing have also been used to study high-intensity laser matter interaction [214], as well as nonlinear ionization dynamics in laser-plasma amplifiers [215].

Another area where high-resolution XUV ptychography may have a significant impact is biological imaging. In particular, the water-window spectral range provides natural contrast for imaging carbon-based structures in an aqueous environment. This contrast mechanism has been established using imaging experiments with synchrotrons and plasma-based soft-X-ray sources (see e.g. [216,217]), also including ptychography [39,218]. While phase-matched HHG sources have been demonstrated in this wavelength range and beyond [82,219,220], limited flux combined with low scattering contrast result in high-resolution tabletop ptychography still being an outstanding challenge. That ptychographic bio-imaging is also possible at longer XUV wavelengths was shown by Baksh et al. [181], who imaged fixed neuronal structures at high spatial resolution, and demonstrated excellent correlation with super-resolution fluorescence microscopy while obtaining complementary structural information in a label-free measurement (see Fig. 10(c)).

The application perspective of ptychography with HHG sources is bright, as it enables XUV imaging with a compact, laboratory-based tabletop setup, which has large advantages in terms of versatility and availability, but also facilitates industrial adoption of the technology. At various synchrotron facilities, ptychography beamlines have been established that are already serving a large and varied scientific and industrial community. Advances in HHG source development are now starting to enable HHG-based ptychography as well, and especially in the industrially relevant wavelength range around 13.5 nm advanced imaging platforms are being developed [179,221,222].

4.4. Towards 3D imaging

Aside from specific applications such as characterization of surfaces and thin films, the ability to image objects in three dimensions is of crucial importance. To date, 3D ptychography has been performed in various forms. Ptychographic X-ray computed tomography (PXCT) was the first three-dimensional ptychography technique that was demonstrated [223–225]. In PXCT the sample translation stage is complemented by an additional rotation stage, allowing to illuminate a 3D sample of interest from different directions. At each sample rotation a complete lateral 2D ptychography scan is performed. At hard x-rays, where multiple scattering of small volumina may

Optics EXPRESS

be neglected, PXCT thus measures a sequence of projections which may be put together using techniques from ordinary computed tomography to produce a 3D image of a sample of interest. At XUV radiation, PXCT has so far not been implemented. Both the high absorption of most samples and multiple scattering effects make PXCT appreciably more challenging with XUV radiation as compared to hard x-rays. Another approach to 3D imaging is multislice ptychography [153]. This approach uses the beam propagation method (BPM) which treats 3D specimens as a sequence of 2D layers, each of which scatter only in the forward direction. With visible light, up to 34 individual slices could be reconstructed and a combination of multislice ptychography and PXCT has been proposed, allowing for scattering inside the sample [153,155,226]. For multislice ptychography the axial slice separation capability of ptychography is on the order of the depth of field (DoF), which scales with λ/NA_d^2. Features separated by axial distances smaller than the DoF appear within the same slice or cross-talk between slices [154]. Thus we believe multislice ptychography at XUV wavelengths has a limited application perspective on only carefully selected specimens, consisting of multiple layers separated by a distance larger than the DoF. To illustrate this, at an XUV wavelength of 13.5 nm and a detection NA of 0.4, the layer separation should at least be 100 nm. We note that interlayer cross-talk is a continuous effect [154] and to get rid of it several hundreds of nanometers slice separation would be beneficial.

Another promising approach is ptychographic optical coherence tomography (POCT) [227]. Here a sequence of reflection-mode ptychography scans are carried out under variation of the probe wavelength. Similar to frequency-domain optical coherence tomography (fd-OCT), this approach allows to transform the reconstructions at each wavelength into a depth-resolved stack of images. POCT is neither a point-scanning, nor a full-field OCT technique. Instead, an extended probe in POCT is somewhat in between point-scanning and full field OCT, while a separate interferometric reference arm is replaced by the computational phase retrieval capability of ptychography (see [228] for a recent comprehensive overview of OCT modalities). Unlike multislice ptychography, in POCT the depth resolution is driven by a broad spectral bandwidth of the source and uncoupled from the detection NA. The resulting axial resolution, in the context of OCT often called *coherence gate*, can be orders of magnitude smaller than the depth of field. Coherence tomography in the XUV has already been demonstrated [229–232]. By combining a broadband illumination in a reflection geometry with a grating spectrometer, impressive axial resolutions (24 nm) have already been achieved. In these demonstrations, the lateral resolution was however limited by the spotsize (20 μm). In POCT, the spot is deconvolved from the sample. However, in POCT the probe is monochromatic requiring wavelength scanning. While the latter step is easily carried out using a visible light or near-infrared swept-source, it remains a challenge to transfer the technique to XUV wavelengths. However, broadband diffraction data can be monochromatized by using XUV Fourier transform spectroscopy, as for instance reported in [126,127]. In addition, recent progress in wavelength control over HHG sources [125] may open up routes towards POCT at XUV wavelengths.

5. Conclusion

Advances in imaging technology have been a driver for new scientific discovery. Ptychographic XUV imaging may well play a similar role, given the omnipresence of complex nanostructures in both science and industry. Especially the quantitative imaging ability of ptychography may prove important for metrology and diagnostic applications. In addition to the need for quantitatively accurate imaging tools, the two main technical ingredients that have enabled the emergence of XUV tabletop ptychography, are the rapid development of coherent imaging techniques, and the significant advances in coherent flux generation from HHG sources in the last decade. Ptychography with HHG sources opens up an array of scientific opportunities, such as the sensitivity for ultrafast phenomena, depth-resolved imaging, and element-specific analysis of thin specimens (transmission-mode) and surfaces (reflection-mode). The advent of

Optics EXPRESS

fast XUV-sensitive CMOS cameras (see section 2.5) opens up new possibilities towards fast data acquisition. Looking at all the progress so far, we identify four elements that will likely play a key role in advancing XUV ptychography development in the next decade: (1) High-flux HHG sources that enable high-resolution tabletop bio-imaging at soft-x-ray photon energies, including the water window. (2) Energy-resolved transmission- and reflection-mode ptychography for element-specific imaging. (3) XUV illumination engineering techniques to enable the generation of structured and tailored beams at high illumination NA. Such XUV beam structuring will facilitate phase contrast imaging on weakly scattering samples, and is important for fast and robust multispectral ptychography. (4) Three-dimensional ptychography (POCT) using tabletop XUV sources. As technology develops along these lines, the capabilities of XUV ptychography will continuously improve. We expect both scientific applications and industrial metrology to greatly benefit from such improvements, as XUV table-top ptychography gradually moves from proof-of-concept experiments towards a general tool for high-resolution quantitative imaging.

Funding. European Research Council (ERC-CoG 864016); Helmholtz Association (FISCOV); Helmholtz Association (incubator project Ptychography 4.0); Fraunhofer-Gesellschaft (Cluster of Excellence Advanced Photon Sources).

Acknowledgments. We would like to thank M. Lottmann for assistance in generating Fig. 5.

Disclosures. The authors declare no conflicts of interest.

Data Availability. The data and code underlying the results presented in Fig. 7 are publicly available [120].

References

1. D. Attwood and A. Sakdinawat, *Soft X-Rays and Extreme Ultraviolet Radiation* (Cambridge University Press, 2017), 2nd ed.
2. F. Krausz and M. Ivanov, "Attosecond physics," Rev. Mod. Phys. **81**(1), 163–234 (2009).
3. P. M. Kraus, M. Zürch, S. K. Cushing, D. M. Neumark, and S. R. Leone, "The ultrafast X-ray spectroscopic revolution in chemical dynamics," Nat. Rev. Chem. **2**(6), 82–94 (2018).
4. A. McPherson, G. Gibson, H. Jara, U. Johann, T. S. Luk, I. A. McIntyre, K. Boyer, and C. K. Rhodes, "Studies of multiphoton production of vacuum-ultraviolet radiation in the rare gases," J. Opt. Soc. Am. B **4**(4), 595 (1987).
5. M. Ferray, A. L'Huillier, and X. Li, "Multiple-harmonic conversion of 1064 nm radiation in rare gases," J. Phys. B: At., Mol. Opt. Phys. **21**(3), L31–L35 (1988).
6. T. Ditmire, E. T. Gumbrell, R. A. Smith, J. W. Tisch, D. D. Meyerhofer, and M. H. Hutchinson, "Spatial coherence measurement of soft x-ray radiation produced by high order harmonic generation," Phys. Rev. Lett. **77**(23), 4756–4759 (1996).
7. R. Zerne, C. Altucci, M. Bellini, M. B. Gaarde, T. W. Hänsch, A. L'Huillier, C. Lyngå, and C. G. Wahlström, "Phase-locked high-order harmonic sources," Phys. Rev. Lett. **79**(6), 1006–1009 (1997).
8. R. A. Bartels, A. Paul, H. Green, H. C. Kapteyn, M. M. Murnane, S. Backus, I. P. Christov, Y. Liu, D. Attwood, and C. Jacobsen, "Generation of spatially coherent light at extreme ultraviolet wavelengths," Science **297**(5580), 376–378 (2002).
9. J. M. Rodenburg, A. C. Hurst, A. G. Cullis, B. R. Dobson, F. Pfeiffer, O. Bunk, C. David, K. Jefimovs, and I. Johnson, "Hard-X-Ray Lensless Imaging of Extended Objects," Phys. Rev. Lett. **98**(3), 034801 (2007).
10. J. Rodenburg and A. Maiden, "Ptychography," in *Springer Handbook of Microscopy*, (Springer, 2019), p. 2.
11. M. D. Seaberg, B. Zhang, D. F. Gardner, E. R. Shanblatt, M. M. Murnane, H. C. Kapteyn, and D. E. Adams, "Tabletop nanometer extreme ultraviolet imaging in an extended reflection mode using coherent Fresnel ptychography," Optica **1**(1), 39 (2014).
12. J. A. Trail and R. L. Byer, "Compact scanning soft-x-ray microscope using a laser-produced plasma source and normal-incidence multilayer mirrors," Opt. Lett. **14**(11), 539 (1989).
13. M. Wieland, C. Spielmann, U. Kleineberg, T. Westerwalbesloh, U. Heinzmann, and T. Wilhein, "Toward time-resolved soft X-ray microscopy using pulsed fs-high-harmonic radiation," Ultramicroscopy **102**(2), 93–100 (2005).
14. R. Früke, J. Kutzner, T. Witting, H. Zacharias, and T. H. Wilhein, "EUV scanning transmission microscope operating with high-harmonic and laser plasma radiation," Europhys. Lett. **72**(6), 915–921 (2005).
15. G. Vaschenko, F. Brizuela, C. Brewer, M. Grisham, H. Mancini, C. S. Menoni, M. C. Marconi, J. J. Rocca, W. Chao, J. A. Liddle, E. H. Anderson, D. T. Attwood, A. V. Vinogradov, I. A. Artioukov, Y. P. Pershyn, and V. V. Kondratenko, "Nanoimaging with a compact extreme-ultraviolet laser," Opt. Lett. **30**(16), 2095 (2005).
16. F. Brizuela, G. Vaschenko, C. Brewer, M. Grisham, C. S. Menoni, M. C. Marconi, J. J. Rocca, W. Chao, J. A. Liddle, E. H. Anderson, D. T. Attwood, A. V. Vinogradov, I. A. Artioukov, Y. P. Pershyn, and V. V. Kondratenko, "Reflection mode imaging with nanoscale resolution using a compact extreme ultraviolet laser," Opt. Express **13**(11), 3983–3988 (2005).

Optics EXPRESS

17. G. Vaschenko, C. Brewer, F. Brizuela, Y. Wang, M. A. Larotonda, B. M. Luther, M. C. Marconi, J. J. Rocca, C. S. Menoni, E. H. Anderson, W. Chao, B. D. Harteneck, J. A. Liddle, Y. Liu, and D. T. Attwood, "Sub-38 nm resolution tabletop microscopy with 13 nm wavelength laser light," Opt. Lett. **31**(9), 1214 (2006).
18. P. W. Wachulak, A. Bartnik, and H. Fiedorowicz, "Sub-70 nm resolution tabletop microscopy at 13.8 nm using a compact laser–plasma EUV source," Opt. Lett. **35**(14), 2337 (2010).
19. J. Pawley, *Handbook of biological confocal microscopy*, vol. 236 (Springer Science & Business Media, 2006).
20. L. Schermelleh, R. Heintzmann, and H. Leonhardt, "A guide to super-resolution fluorescence microscopy," (2010).
21. D. Paganin, *Coherent X-Ray Optics* (Oxford University Press, 2006), 1st ed.
22. J. Miao, P. Charalambous, and J. Kirz, "Extending the methodology of X-ray crystallography to allow imaging of micrometre-sized non-crystalline specimens," Nature **400**(6742), 342–344 (1999).
23. R. L. Sandberg, A. Paul, D. A. Raymondson, S. Hädrich, D. M. Gaudiosi, J. Holtsnider, R. I. Tobey, O. Cohen, M. M. Murnane, H. C. Kapteyn, C. Song, J. Miao, Y. Liu, and F. Salmassi, "Lensless diffractive imaging using tabletop coherent high-harmonic soft-X-ray beams," Phys. Rev. Lett. **99**(9), 098103 (2007).
24. J. Miao, T. Ishikawa, I. K. Robinson, and M. M. Murnane, "Beyond crystallography: Diffractive imaging using coherent x-ray light sources," Science **348**(6234), 530–535 (2015).
25. J. R. Fienup, "Phase retrieval algorithms: a comparison," Appl. Opt. **21**(15), 2758–2769 (1982).
26. S. Marchesini, H. He, H. N. Chapman, S. P. Hau-Riege, A. Noy, M. R. Howells, U. Weierstall, and J. C. H. Spence, "X-ray image reconstruction from a diffraction pattern alone," Phys. Rev. B **68**(14), 140101 (2003).
27. J. R. Fienup, "Phase retrieval algorithms: a personal tour," Appl. Opt. **52**(1), 45–56 (2013).
28. Y. Shechtman, Y. C. Eldar, O. Cohen, H. N. Chapman, J. Miao, and M. Segev, "Phase Retrieval with Application to Optical Imaging: A contemporary overview," IEEE Signal Process. Mag. **32**(3), 87–109 (2015).
29. J. Vila-Comamala, A. Diaz, M. Guizar-Sicairos, A. Mantion, C. M. Kewish, A. Menzel, O. Bunk, and C. David, "Characterization of high-resolution diffractive X-ray optics by ptychographic coherent diffractive imaging," Opt. Express **19**(22), 21333 (2011).
30. A. Schropp, R. Hoppe, V. Meier, J. Patommel, F. Seiboth, H. J. Lee, B. Nagler, E. C. Galtier, B. Arnold, U. Zastrau, J. B. Hastings, D. Nilsson, F. Uhlén, U. Vogt, H. M. Hertz, and C. G. Schroer, "Full spatial characterization of a nanofocused X-ray free-electron laser beam by ptychographic imaging," Sci. Rep. **3**(1), 1633 (2013).
31. J. Vila-Comamala, A. Sakdinawat, and M. Guizar-Sicairos, "Characterization of x-ray phase vortices by ptychographic coherent diffractive imaging," Opt. Lett. **39**(18), 5281 (2014).
32. L. Loetgering, M. Baluktsian, K. Keskinbora, R. Horstmeyer, T. Wilhein, G. Schütz, K. S. Eikema, and S. Witte, "Generation and characterization of focused helical x-ray beams," Sci. Adv. **6**(7), eaax8836 (2020).
33. M. Du, L. Loetgering, K. Eikema, and S. Witte, "Measuring laser beam quality, wavefronts, and lens aberrations using ptychography," Opt. Express **28**(4), 5022–5034 (2020).
34. P. Thibault, M. Dierolf, A. Menzel, O. Bunk, C. David, and F. Pfeiffer, "High-Resolution Scanning X-ray Diffraction Microscopy," Science **321**(5887), 379–382 (2008).
35. F. Pfeiffer, "X-ray ptychography," Nat. Photonics **12**(1), 9–17 (2018).
36. K. Giewekemeyer, P. Thibault, S. Kalbfleisch, A. Beerlink, C. M. Kewish, M. Dierolf, F. Pfeiffer, and T. Salditt, "Quantitative biological imaging by ptychographic x-ray diffraction microscopy," Proc. Natl. Acad. Sci. U. S. A. **107**(2), 529–534 (2010).
37. J. Marrison, L. Räty, P. Marriott, and P. O'Toole, "Ptychography–a label free, high-contrast imaging technique for live cells using quantitative phase information," Sci. Rep. **3**(1), 2369 (2013).
38. N. Anthony, G. Cadenazzi, H. Kirkwood, E. Huwald, K. Nugent, and B. Abbey, "A Direct Approach to In-Plane Stress Separation using Photoelastic Ptychography," Sci. Rep. **6**(1), 30541 (2016).
39. M. Rose, T. Senkbeil, A. R. von Gundlach, S. Stuhr, C. Rumancev, D. Dzhigaev, I. Besedin, P. Skopintsev, L. Loetgering, J. Viefhaus, A. Rosenhahn, and I. A. Vartanyants, "Quantitative ptychographic bio-imaging in the water window," Opt. Express **26**(2), 1237–1254 (2018).
40. D. Popmintchev, C. Hernández-García, F. Dollar, C. Mancuso, J. A. Pérez-Hernández, M. C. Chen, A. Hankla, X. Gao, B. Shim, A. L. Gaeta, M. Tarazkar, D. A. Romanov, R. J. Levis, J. A. Gaffney, M. Foord, S. B. Libby, A. Jaron-Becker, A. Becker, L. Plaja, M. M. Murnane, H. C. Kapteyn, and T. Popmintchev, "Ultraviolet surprise: Efficient soft X-ray high-harmonic generation in multiply ionized plasmas," Science **350**(6265), 1225–1231 (2015).
41. S. Hädrich, J. Rothhardt, M. Krebs, S. Demmler, A. Klenke, A. Tünnermann, and J. Limpert, "Single-pass high harmonic generation at high repetition rate and photon flux," (2016).
42. R. Klas, A. Kirsche, M. Gebhardt, J. Buldt, H. Stark, S. Hädrich, J. Rothhardt, and J. Limpert, "Ultra-short-pulse high-average-power megahertz-repetition-rate coherent extreme-ultraviolet light source," PhotoniX **2**(1), 4–8 (2021).
43. I. Pupeza, C. Zhang, M. Högner, and J. Ye, "Extreme-ultraviolet frequency combs for precision metrology and attosecond science," Nat. Photonics **15**(3), 175–186 (2021).
44. T. Krücken, K. Bergmann, L. Juschkin, and R. Lebert, "Fundamentals and limits for the EUV emission of pinch plasma sources for EUV lithography," J. Phys. D: Appl. Phys. **37**(23), 3213–3224 (2004).
45. O. O. Versolato, "Physics of laser-driven tin plasma sources of EUV radiation for nanolithography," Plasma Sources Sci. Technol. **28**(8), 083001 (2019).
46. V. Bakshi, *EUV sources for lithography*, vol. 149 (SPIE press, 2006).
47. D. Schäfer, K. Bergmann, M. Benk, and T. Wilhein, "Compact soft x-ray microscope using a gas-discharge light source," Opt. Lett. **33**(20), 2359–2361 (2008).

Optics EXPRESS

48. M. Banyay and L. Juschkin, "Table-top reflectometer in the extreme ultraviolet for surface sensitive analysis," Appl. Phys. Lett. **94**(6), 063507 (2009).
49. M. Van Den Brink, "Continuing to shrink: Next-generation lithography - Progress and prospects," Dig. Tech. Pap. - IEEE Int. Solid-State Circuits Conf. **56**, 20–25 (2013).
50. M. Odstrcil, J. Bussmann, D. Rudolf, R. Bresenitz, J. Miao, W. S. Brocklesby, and L. Juschkin, "Ptychographic imaging with a compact gas–discharge plasma extreme ultraviolet light source," Opt. Lett. **40**(23), 5574 (2015).
51. A. Jonas, H. Stiel, L. Glöggler, D. Dahm, K. Dammer, B. Kanngießer, and I. Mantouvalou, "Towards Poisson noise limited optical pump soft X-ray probe NEXAFS spectroscopy using a laser-produced plasma source," Opt. Express **27**(25), 36524–36537 (2019).
52. J. Bußmann, M. Odstrčil, Y. Teramoto, and L. Juschkin, "Ptychographic imaging with partially coherent plasma EUV sources," Adv. Opt. Technol. **6**(6), 459–466 (2017).
53. D. J. Batey, F. Van Assche, S. Vanheule, M. N. Boone, A. J. Parnell, O. O. Mykhaylyk, C. Rau, and S. Cipiccia, "X-Ray Ptychography with a Laboratory Source," Phys. Rev. Lett. **126**(19), 193902 (2021).
54. F. J. Furch, B. A. Reagan, B. M. Luther, A. H. Curtis, S. P. Meehan, and J. J. Rocca, "Demonstration of an all-diode-pumped soft x-ray laser," Opt. Lett. **34**(21), 3352–3354 (2009).
55. P. Zeitoun, G. Faivre, S. Sebban, T. Mocek, A. Hallou, M. Fajardo, D. Aubert, P. Balcou, F. Burgy, D. Douillet, S. Kazamias, G. Lachèze-Murel, T. Lefrou, S. Le Pape, P. Mercere, H. Merdji, A. S. Merlens, J. P. Rousseau, and C. Valentin, "A high-intensity highly coherent soft X-ray femtosecond laser seeded by a high harmonic beam," Nature **431**(7007), 426–429 (2004).
56. B. Ecker, B. Aurand, D. C. Hochhaus, P. Neumayer, B. Zielbauer, E. Oliva, L. Li, T. T. T. Le, Q. Jin, H. Zhao, K. Cassou, S. Daboussi, O. Guilbaud, S. Kazamias, D. Ros, P. Zeitoun, and T. Kuehl, "Double-stage soft x-ray laser pumped by multiple pulses applied in grazing incidence," J. Phys. B: At., Mol. Opt. Phys. **48**(14), 144009 (2015).
57. B. A. Reagan, Y. Wang, D. Alessi, K. Wernsing, B. M. Luther, M. A. Curtis, M. Berrill, D. Martz, S. Wang, L. Yin, F. Furch, M. Woolston, D. Patel, V. N. Shlyaptsev, C. S. Menoni, and J. J. Rocca, "Demonstration of a 100 Hz repetition rate soft x-ray laser and gain-saturated sub-10 nm table-top lasers," Springer Proc. Phys. **147**, 215–225 (2014).
58. M. Zürch, R. Jung, C. Späth, J. Tümmler, A. Guggenmos, D. Attwood, U. Kleineberg, H. Stiel, and C. Spielmann, "Transverse Coherence Limited Coherent Diffraction Imaging using a Molybdenum Soft X-ray Laser Pumped at Moderate Pump Energies," Sci. Rep. **7**(1), 5314 (2017).
59. P. Corkum, "Plasma perspective on strong field multiphoton ionization," Phys. Rev. Lett. **71**(13), 1994–1997 (1993).
60. Z. Chang, *Fundamentals of Attosecond Optics* (CRC Press, Boca Raton, Florida, 2011).
61. J. Rothhardt, S. Hädrich, Y. Shamir, M. Tschnernajew, R. Klas, A. Hoffmann, G. K. G. Tadesse, A. Klenke, T. Gottschall, T. Eidam, R. Boll, C. Bomme, H. Dachraoui, B. Erk, M. Di Fraia, D. A. D. Horke, T. Kierspel, T. Mullins, A. Przystawik, E. Savelyev, J. Wiese, T. Laarmann, J. Küpper, D. Rolles, J. Limpert, A. Tünnermann, R. Boll, C. Bomme, H. Dachraoui, B. Erk, M. D. Fraia, D. A. D. Horke, T. Kierspel, T. Mullins, A. Przystawik, E. Savelyev, J. Wiese, T. Laarmann, J. Küpper, D. Rolles, M. Di Fraia, D. A. D. Horke, T. Kierspel, T. Mullins, A. Przystawik, E. Savelyev, J. Wiese, T. Laarmann, J. Küpper, D. Rolles, J. Limpert, and A. Tünnermann, "High-repetition-rate and high-photon-flux 70 eV high-harmonic source for coincidence ion imaging of gas-phase molecules," Opt. Express **24**(16), 18133–18147 (2016).
62. J. Rothhardt, M. Krebs, S. Hädrich, S. Demmler, J. Limpert, and A. Tünnermann, "Absorption-limited and phase-matched high harmonic generation in the tight focusing regime," New J. Phys. **16**(3), 033022 (2014).
63. E. Constant, D. Garzella, P. Breger, E. Mével, C. Dorrer, C. Le Blanc, F. Salin, and P. Agostini, "Optimizing High Harmonic Generation in Absorbing Gases: Model and Experiment," Phys. Rev. Lett. **82**(8), 1668–1671 (1999).
64. R. Klas, S. Demmler, M. Tschernajew, S. Hädrich, Y. Shamir, A. Tünnermann, J. Rothhardt, and J. Limpert, "Table-Top Milliwatt-Class Extreme Ultraviolet High Harmonic Light Source," Optica **3**(11), 1167–1170 (2016).
65. E. Seres, J. Seres, and C. Spielmann, "Extreme ultraviolet light source based on intracavity high harmonic generation in a mode locked Ti:sapphire oscillator with 9.4 MHz repetition rate," Opt. Express **20**(6), 6185–6190 (2012).
66. F. Labaye, M. Gaponenko, V. J. Wittwer, A. Diebold, C. Paradis, N. Modsching, L. Merceron, F. Emaury, I. J. Graumann, C. R. Phillips, C. J. Saraceno, C. Kränkel, U. Keller, and T. Südmeyer, "Extreme ultraviolet light source at a megahertz repetition rate based on high-harmonic generation inside a mode-locked thin-disk laser oscillator," Opt. Lett. **42**(24), 5170 (2017).
67. J. Fischer, J. Drs, F. Labaye, N. Modsching, V. J. Wittwer, and T. Südmeyer, "Intra-oscillator high harmonic generation in a thin-disk laser operating in the 100-fs regime," Opt. Express **29**(4), 5833 (2021).
68. H. Wang, Y. Xu, S. Ulonska, J. S. Robinson, P. Ranitovic, and R. A. Kaindl, "Bright high-repetition-rate source of narrowband extreme-ultraviolet harmonics beyond 22 eV," Nat. Commun. **6**(1), 7459 (2015).
69. A. Cingöz, D. C. Yost, T. K. Allison, A. Ruehl, M. E. Fermann, I. Hartl, and J. Ye, "Direct frequency comb spectroscopy in the extreme ultraviolet," Nature **482**(7383), 68–71 (2012).
70. G. Porat, C. M. Heyl, S. B. Schoun, C. Benko, N. Dörre, K. L. Corwin, and J. Ye, "Phase-matched extreme-ultraviolet frequency-comb generation," Nat. Photonics **12**(7), 387–391 (2018).
71. I. Pupeza, S. Holzberger, T. Eidam, H. Carstens, D. Esser, J. Weitenberg, P. Rußbüldt, J. Rauschenberger, J. Limpert, T. Udem, A. Tünnermann, T. W. Hänsch, A. Apolonski, F. Krausz, and E. Fill, "Compact high-repetition-rate source of coherent 100 eV radiation," Nat. Photonics **7**(8), 608–612 (2013).

Optics EXPRESS

72. J. P. Brichta, M. C. Wong, J. B. Bertrand, H. C. Bandulet, D. M. Rayner, and V. R. Bhardwaj, "Comparison and real-time monitoring of high-order harmonic generation in different sources," Phys. Rev. A **79**(3), 033404 (2009).
73. S. L. Cousin, F. Silva, S. Teichmann, M. Hemmer, B. Buades, and J. Biegert, "High-flux table-top soft x-ray source driven by sub-2-cycle, CEP stable, 1. 85- μ m 1-kHz pulses for carbon K-edge spectroscopy," Opt. Lett. **39**(18), 5383–5386 (2014).
74. C. Ding, W. Xiong, T. Fan, D. D. Hickstein, T. Popmintchev, X. Zhang, M. Walls, M. M. Murnane, and H. C. Kapteyn, "High flux coherent super-continuum soft X-ray source driven by a single-stage, 10mJ, Ti:sapphire amplifier-pumped OPA," Opt. Express **22**(5), 6194 (2014).
75. J. Hüve, T. Haarlammert, T. Steinbrück, J. Kutzner, G. Tsilimis, and H. Zacharias, "High-flux high harmonic soft X-ray generation up to 10 kHz repetition rate," Opt. Commun. **266**(1), 261–265 (2006).
76. A. S. Johnson, D. R. Austin, D. A. Wood, C. Brahms, A. Gregory, K. B. Holzner, S. Jarosch, E. W. Larsen, S. Parker, C. S. Strüber, P. Ye, J. W. G. Tisch, and J. P. Marangos, "High-flux soft x-ray harmonic generation from ionization-shaped few-cycle laser pulses," Sci. Adv. **4**(5), eaar3761 (2018).
77. D. Popmintchev, B. R. Galloway, M. C. Chen, F. Dollar, C. A. Mancuso, A. Hankla, L. Miaja-Avila, G. O'Neil, J. M. Shaw, G. Fan, S. Ališauskas, G. Andriukaitis, T. Balčiunas, O. D. Mücke, A. Pugzlys, A. Baltuška, H. C. Kapteyn, T. Popmintchev, and M. M. Murnane, "Near- and Extended-Edge X-Ray-Absorption Fine-Structure Spectroscopy Using Ultrafast Coherent High-Order Harmonic Supercontinua," Phys. Rev. Lett. **120**(9), 093002 (2018).
78. A. Rundquist, C. G. Durfee, Z. Chang, C. Herne, S. Backus, M. M. Murnane, and H. C. Kapteyn, "Phase-Matched Generation of Coherent Soft X-rays," Science **280**(5368), 1412–1415 (1998).
79. E. Takahashi, Y. Nabekawa, and K. Midorikawa, "Generation of 10- microJ coherent extreme-ultraviolet light by use of high-order harmonics," Opt. Lett. **27**(21), 1920–1922 (2002).
80. R. Klas, W. Eschen, A. Kirsche, J. Rothhardt, and J. Limpert, "Generation of coherent broadband high photon flux continua in the XUV with a sub- two-cycle fiber laser," Opt. Express **28**(5), 6188–6196 (2020).
81. M. Tschernajew, S. Hädrich, R. Klas, M. Gebhardt, R. Horsten, S. Weerdenburg, S. Pyatchenkov, W. Coene, J. Rothhardt, T. Eidam, and J. Limpert, "High Repetition Rate High Harmonic Generation with Ultra-high Photon Flux," in *Laser Congress 2020 (ASSL, LAC)*, (Optical Society of America, 2020), p. JTh2A.21.
82. M. Gebhardt, T. Heuermann, R. Klas, C. Liu, A. Kirsche, M. Lenski, Z. Wang, C. Gaida, J. E. Antonio-Lopez, A. Schülzgen, R. Amezcua-Correa, J. Rothhardt, and J. Limpert, "Bright, high repetition rate water window soft X-ray source enabled by nonlinear pulse self-compression in antiresonant hollow-core fibre," Light: Sci. Appl. **10**(1), 36 (2021).
83. S. Hädrich, A. Klenke, J. Rothhardt, M. Krebs, A. Hoffmann, O. Pronin, V. Pervak, J. Limpert, and A. Tünnermann, "High photon flux table-top coherent extreme ultraviolet source," Nat. Photonics **8**(10), 779–783 (2014).
84. A. Comby, D. Descamps, S. Beauvarlet, A. Gonzalez, F. Guichard, S. Petit, Y. Zaouter, and Y. Mairesse, "Cascaded harmonic generation from a fiber laser: a milliwatt XUV source," Opt. Express **27**(15), 20383 (2019).
85. A. Rose, *Vision: human and electronic* (Springer Science & Business Media, 2013).
86. M. R. Howells, T. Beetz, H. N. Chapman, C. Cui, J. M. Holton, C. J. Jacobsen, J. Kirz, E. Lima, S. Marchesini, H. Miao, D. Sayre, D. a. Shapiro, J. C. H. Spence, and D. Starodub, "An assessment of the resolution limitation due to radiation-damage in x-ray diffraction microscopy," J. Electron Spectrosc. Relat. Phenom. **170**(1-3), 4–12 (2009).
87. Y. Nagata, K. Furusawa, Y. Nabekawa, and K. Midorikawa, "Single-shot spatial-coherence measurement of 13 nm high-order harmonic beam by a Young's double-slit measurement," Opt. Lett. **32**(6), 722 (2007).
88. D. T. Lloyd, K. O'Keeffe, P. N. Anderson, and S. M. Hooker, "Gaussian-Schell analysis of the transverse spatial properties of high-harmonic beams," Sci. Rep. **6**(1), 30504 (2016).
89. J. Duarte, A. I. Gonzalez, R. Cassin, R. Nicolas, M. Kholodstova, W. Boutu, M. Fajardo, and M. Hamed, "Single-shot spatial coherence characterization of x-ray ultrafast sources," Opt. Lett. **46**(7), 1764 (2021).
90. T. Ditmire, J. W. G. Tisch, E. T. Gumbrell, R. A. Smith, D. D. Meyerhofer, and M. H. R. Hutchinson, "Spatial coherence of short wavelength high-order harmonics," Appl. Phys. B **65**(3), 313–328 (1997).
91. E. Wolf, *Introduction to the Theory of Coherence and Polarization of Light* (Cambridge University Press, Cambridge, 2007), 1st ed.
92. H. Jiang, C. Song, C.-C. Chen, R. Xu, K. S. Raines, B. P. Fahimian, C.-H. Lu, T.-K. Lee, A. Nakashima, J. Urano, T. Ishikawa, F. Tamanoi, and J. Miao, "Quantitative 3D imaging of whole, unstained cells by using X-ray diffraction microscopy," Proc. Natl. Acad. Sci. **107**(25), 11234–11239 (2010).
93. B. L. Henke, E. M. Gullikson, and J. C. Davis, "X-ray interactions: photoabsorption, scattering, transmission, and reflection at E = 50–30, 000 eV, Z = 1–92," At. Data Nucl. Data Tables **54**(2), 181–342 (1993).
94. M. Tanksalvala, C. L. Porter, Y. Esashi, B. Wang, N. W. Jenkins, Z. Zhang, G. P. Miley, J. L. Knobloch, B. McBennett, N. Horiguchi, S. Yazdi, J. Zhou, M. N. Jacobs, C. S. Bevis, R. M. Karl, P. Johnsen, D. Ren, L. Waller, D. E. Adams, S. L. Cousin, C. T. Liao, J. Miao, M. Gerrity, H. C. Kapteyn, and M. M. Murnane, "Nondestructive, high-resolution, chemically specific 3D nanostructure characterization using phase-sensitive EUV imaging reflectometry," Sci. Adv. **7**(5), 32–38 (2021).
95. B. Zhang, D. F. Gardner, M. H. Seaberg, E. R. Shanblatt, C. L. Porter, R. Karl, C. A. Mancuso, H. C. Kapteyn, M. M. Murnane, and D. E. Adams, "Ptychographic hyperspectral spectromicroscopy with an extreme ultraviolet high harmonic comb," Opt. Express **24**(16), 18745 (2016).
96. L. Loetgering, X. Liu, A. C. C. De Beurs, M. Du, G. Kuijper, K. S. E. Eikema, and S. Witte, "Tailoring spatial entropy in extreme ultraviolet focused beams for multispectral ptychography," Optica **8**(2), 130–138 (2021).

Optics EXPRESS

97. J. R. Janesick, *Scientific charge-coupled devices*, vol. 83 (SPIE press, 2001).
98. Technologies Andor, "I-Kon-L Datasheet," https://andor.oxinst.com/products/cameras-for-x-ray-euv-electron-and-neutron-detection#.
99. K. Desjardins, H. Popescu, P. Mercère, C. Menneglier, R. Gaudemer, K. Thånell, and N. Jaouen, "Characterization of a back-illuminated CMOS camera for soft x-ray coherent scattering," AIP Conf. Proc. **2054**, 060066 (2019).
100. T. Harada, N. Teranishi, T. Watanabe, Q. Zhou, J. Bogaerts, and X. Wang, "High-exposure-durability, high-quantum-efficiency (>90%) backside-illuminated soft-X-ray CMOS sensor," Appl. Phys. Express **13**(1), 016502 (2020).
101. Andor-Technologies, "Marana-X Datasheet," https://andor.oxinst.com/products/high-energy-detection/marana-x-scmos.
102. Sydor-Technologies, "Wraith - sCMOS Detection Imaging of EUV and Soft X-Rays," https://sydortechnologies.com/wp-content/uploads/SydorTech_WraithBrochure_V0.5.pdf.
103. S.-J. Lee, C. J. Titus, R. Alonso Mori, M. L. Baker, D. A. Bennett, H.-M. Cho, W. B. Doriese, J. W. Fowler, K. J. Gaffney, and A. Gallo, and Others, "Soft X-ray spectroscopy with transition-edge sensors at Stanford Synchrotron Radiation Lightsource beamline 10-1," Rev. Sci. Instrum. **90**(11), 113101 (2019).
104. J. Rothhardt, G. K. Tadesse, W. Eschen, and J. Limpert, "Table-top nanoscale coherent imaging with XUV light," J. Opt. **20**(11), 113001 (2018).
105. B. Abbey, K. A. Nugent, G. J. Williams, J. N. Clark, A. G. Peele, M. A. Pfeifer, M. D. E. Jonge, and I. A. N. M. C. Nulty, "Keyhole coherent diffractive imaging," Nat. Phys. **4**(5), 394–398 (2008).
106. D. J. Vine, G. J. Williams, B. Abbey, M. A. Pfeifer, J. N. Clark, M. D. de Jonge, I. McNulty, A. G. Peele, and K. A. Nugent, "Ptychographic Fresnel coherent diffractive imaging," Phys. Rev. A **80**(6), 063823 (2009).
107. D. W. Noom, D. E. B. Flaes, E. Labordus, K. S. Eikema, and S. Witte, "High-speed multi-wavelength Fresnel diffraction imaging," Opt. Express **22**(25), 30504–30511 (2014).
108. D. Gabor, "A new microscopic principle," Nature **161**(4098), 777–778 (1948).
109. G. W. Stroke, "Lensless Fourier Transform Method For Optical Holography," Appl. Phys. Lett. **6**(10), 201–203 (1965).
110. I. McNulty, J. Kirz, C. Jacobsen, E. H. Anderson, M. R. Howells, and D. P. Kern, "High-Resolution Imaging by Fourier Transform X-ray Holography," Science **256**(5059), 1009–1012 (1992).
111. S. Eisebitt, J. Lüning, W. F. Schlotter, M. Lörgen, O. Hellwig, W. Eberhardt, and J. Stöhr, "Lensless imaging of magnetic nanostructures by X-ray spectro-holography," Nature **432**(7019), 885–888 (2004).
112. J. Miao, D. Sayre, and H. N. Chapman, "Phase retrieval from the magnitude of the Fourier transforms of nonperiodic objects," J. Opt. Soc. Am. A **15**(6), 1662–1669 (1998).
113. J. R. Fienup, "Reconstruction of an object from the modulus of its Fourier transform," Opt. Lett. **3**(1), 27–29 (1978).
114. K. Akiyama and E. al., "First M87 Event Horizon Telescope Results. IV. Imaging the Central Supermassive Black Hole," The Astrophys. J. Lett. **875**(1), L4 (2019).
115. J. R. Fienup, "Reconstruction of a complex-valued object from the modulus of its Fourier transform using a support constraint," J. Opt. Soc. Am. A **4**(1), 118–123 (1987).
116. D. Shapiro, P. Thibault, T. Beetz, V. Elser, M. Howells, C. Jacobsen, J. Kirz, E. Lima, H. Miao, A. M. Neiman, and D. Sayre, "Biological imaging by soft x-ray diffraction microscopy," Proc. Natl. Acad. Sci. U. S. A. **102**(43), 15343–15346 (2005).
117. R. Neutze, R. Wouts, D. Van Der Spoel, E. Weckert, and J. Hajdu, "Potential for biomolecular imaging with femtosecond X-ray pulses," (2000).
118. H. N. Chapman, P. Fromme, A. Barty, T. A. White, R. A. Kirian, A. Aquila, M. S. Hunter, J. Schulz, D. P. Deponte, U. Weierstall, R. B. Doak, F. R. Maia, A. V. Martin, I. Schlichting, L. Lomb, N. Coppola, R. L. Shoeman, S. W. Epp, R. Hartmann, D. Rolles, A. Rudenko, L. Foucar, N. Kimmel, G. Weidenspointner, P. Holl, M. Liang, M. Barthelmess, C. Caleman, S. Boutet, M. J. Bogan, J. Krzywinski, C. Bostedt, S. Bajt, L. Gumprecht, B. Rudek, B. Erk, C. Schmidt, A. Hömke, C. Reich, D. Pietschner, L. Ströder, G. Hauser, H. Gorke, J. Ullrich, S. Herrmann, G. Schaller, F. Schopper, H. Soltau, K. U. Kühnel, M. Messerschmidt, J. D. Bozek, S. P. Hau-Riege, M. Frank, C. Y. Hampton, R. G. Sierra, D. Starodub, G. J. Williams, J. Hajdu, N. Timneanu, M. M. Seibert, J. Andreasson, A. Rocker, O. Jönsson, M. Svenda, S. Stern, K. Nass, R. Andritschke, C. D. Schröter, F. Krasniqi, M. Bott, K. E. Schmidt, X. Wang, I. Grotjohann, J. M. Holton, T. R. Barends, R. Neutze, S. Marchesini, R. Fromme, S. Schorb, D. Rupp, M. Adolph, T. Gorkhover, I. Andersson, H. Hirsemann, G. Potdevin, H. Graafsma, B. Nilsson, and J. C. Spence, "Femtosecond X-ray protein nanocrystallography," Nature **470**(7332), 73–77 (2011).
119. N.-T. D. Loh and V. Elser, "Reconstruction algorithm for single-particle diffraction imaging experiments," Phys. Rev. E **80**(2), 026705 (2009).
120. "Shrink-Wrap," https://github.com/larsloetgering/Shrink-Wrap.
121. D. F. Gardner, B. Zhang, M. D. Seaberg, L. S. Martin, D. E. Adams, F. Salmassi, E. Gullikson, H. Kapteyn, and M. Murnane, "High numerical aperture reflection mode coherent diffraction microscopy using off-axis apertured illumination," Opt. Express **20**(17), 19050 (2012).
122. R. L. Sandberg, C. Song, P. W. Wachulak, D. A. Raymondson, A. Paul, B. Amirbekian, E. Lee, A. E. Sakdinawat, C. La-O-Vorakiat, M. C. Marconi, C. S. Menoni, M. M. Murnane, J. J. Rocca, H. C. Kapteyn, and J. Miao, "High numerical aperture tabletop soft x-ray diffraction microscopy with 70-nm resolution," Proc. Natl. Acad. Sci. **105**(1), 24–27 (2008).

Optics EXPRESS

123. M. Zürch, J. Rothhardt, S. Hädrich, S. Demmler, M. Krebs, J. Limpert, A. Tünnermann, A. Guggenmos, U. Kleineberg, and C. Spielmann, "Real-time and Sub-wavelength Ultrafast Coherent Diffraction Imaging in the Extreme Ultraviolet," Sci. Rep. **4**(1), 7356 (2015).
124. G. K. Tadesse, R. Klas, S. Demmler, S. Hädrich, I. Wahyutama, M. Steinert, C. Spielmann, M. Zürch, T. Pertsch, A. Tünnermann, J. Limpert, and J. Rothhardt, "High speed and high resolution table-top nanoscale imaging," Opt. Lett. **41**(22), 5170 (2016).
125. V. Schuster, V. Hilbert, R. Klas, C. Liu, M. Tschernajew, B. Bernhardt, J. Rothhardt, and J. Limpert, "Agile spectral tuning of high order harmonics by interference of two driving pulses," Opt. Express **29**(14), 22117 (2021).
126. S. Witte, V. T. Tenner, D. W. E. Noom, and K. S. E. Eikema, "Lensless diffractive imaging with ultra-broadband table-top sources: from infrared to extreme-ultraviolet wavelengths," Light: Sci. Appl. **3**(3), e163 (2014).
127. G. S. M. Jansen, D. Rudolf, L. Freisem, K. S. E. Eikema, and S. Witte, "Spatially resolved Fourier transform spectroscopy in the extreme ultraviolet," Optica **3**(10), 1122–1125 (2016).
128. G. S. M. Jansen, A. de Beurs, X. Liu, K. S. E. Eikema, and S. Witte, "Diffractive shear interferometry for extreme ultraviolet high-resolution lensless imaging," Opt. Express **26**(10), 12479–12489 (2018).
129. A. C. C. de Beurs, A. P. Konijnenberg, G. S. M. Jansen, K. S. E. Eikema, S. Witte, W. M. J. Coene, X. Liu, G. S. M. Jansen, A. P. Konijnenberg, A. P. Konijnenberg, W. M. J. Coene, W. M. J. Coene, K. S. E. Eikema, K. S. E. Eikema, S. Witte, S. Witte, and S. Witte, "Extreme ultraviolet lensless imaging without object support through rotational diversity in diffractive shearing interferometry," Opt. Express **28**(4), 5257–5266 (2020).
130. J. C. H. Spence, U. Weierstall, and M. Howells, "Coherence and sampling requirements for diffractive imaging," Ultramicroscopy **101**(2-4), 149–152 (2004).
131. F. van der Veen and F. Pfeiffer, "Coherent x-ray scattering," J. Phys.: Condens. Matter **16**, 5003 (2004).
132. S. Marchesini, "Invited Article : A unified evaluation of iterative projection algorithms for phase retrieval," Rev. Sci. Instrum. **78**(1), 011301 (2007).
133. V. Elser, I. Rankenburg, and P. Thibault, "Searching with iterated maps," Proc. Natl. Acad. Sci. **104**(2), 418–423 (2007).
134. H. N. Chapman and K. A. Nugent, "Coherent lensless X-ray imaging," Nat. Photonics **4**(12), 833–839 (2010).
135. J. C. H. Spence, "Diffractive Imaging of Single Particles," in *Springer Handbook of Microscopy*, (Springer, 2019), pp. 1009–1036.
136. J. Z. Young and F. Roberts, "A Flying-spot Microscope," Nature **167**(4241), 231 (1951).
137. H. H. Pattee, "The scanning x-ray microscope," J. Opt. Soc. Am. **43**(1), 61–62 (1953).
138. P. O. Montgomery, F. Roberts, and W. Bonner, "The Flying-Spot Monochromatic Ultra-Violet Television Microscope," Nature **177**(4521), 1172 (1956).
139. V. E. Cosslett and P. Duncumb, "Micro-analysis by a Flying-Spot X-Ray Method," Nature **177**(4521), 1172–1173 (1956).
140. P. Horowitz and J. A. Howell, "A scanning x-ray microscope using synchrotron radiation," Science **178**(4061), 608–611 (1972).
141. T. Wilson and C. Sheppard, *Theory and practice of scanning optical microscopy*, vol. 180 (Academic Press London, 1984).
142. P. Thibault, M. Dierolf, C. M. Kewish, A. Menzel, O. Bunk, and F. Pfeiffer, "Contrast mechanisms in scanning transmission x-ray microscopy," Phys. Rev. A **80**(4), 043813 (2009).
143. H. Rarback, J. M. Kenney, J. Kirz, M. R. Howells, P. Chang, P. J. Coane, R. Feder, P. J. Houzego, D. P. Kern, and D. Sayre, "Recent results from the Stony Brook scanning microscope," in *X-ray Microscopy*, (Springer, 1984), pp. 203–216.
144. J. M. Kenney, J. Kirz, H. Rarback, M. R. Howells, P. Chang, P. J. Coane, R. Feder, P. J. Houzego, D. P. Kern, and D. Sayre, "Soft X-ray microscopy at the NSLS," Nucl. Instruments Methods Phys. Res. **222**(1-2), 37–41 (1984).
145. C. Jacobsen, S. Williams, E. Anderson, M. T. Browne, C. J. Buckley, D. Kern, J. Kirz, M. Rivers, and X. Zhang, "Diffraction-limited imaging in a scanning transmission x-ray microscope," Opt. Commun. **86**(3-4), 351–364 (1991).
146. H. N. Chapman, "Phase-retrieval X-ray microscopy by Wigner-distribution deconvolution," Ultramicroscopy **66**(3-4), 153–172 (1996).
147. W. J. Eaton, G. R. Morrison, and N. R. Waltham, "Configured detector system for STXM imaging," AIP Conf. Proc. **507**, 452–457 (2000).
148. M. Howells, C. Jacobsen, T. Warwick, and A. den Bos, "Principles and applications of zone plate X-ray microscopes," in *Science of microscopy*, (Springer, 2007), pp. 835–926.
149. M. D. De Jonge, C. G. Ryan, and C. J. Jacobsen, "X-ray nanoprobes and diffraction-limited storage rings: Opportunities and challenges of fluorescence tomography of biological specimens," J. Synchrotron Radiat. **21**(5), 1031–1047 (2014).
150. M. O. Krause, "Atomic radiative and radiationless yields for K and L shells," J. Phys. Chem. Ref. Data **8**(2), 307–327 (1979).
151. B. Kaulich, A. Gianoncelli, A. Beran, D. Eichert, I. Kreft, P. Pongrac, M. Regvar, K. Vogel-Miku, and M. Kiskinova, "Low-energy X-ray fluorescence microscopy opening new opportunities for bio-related research," J. R. Soc. Interface. **6**(suppl_5), 1 (2009).

Optics EXPRESS

152. T. Helk, E. Berger, S. Jamnuch, L. Hoffmann, A. Kabacinski, J. Gautier, F. Tissandier, J.-P. Goddet, H.-T. Chang, J. Oh, C. D. Pemmaraju, T. A. Pascal, S. Sebban, C. Spielmann, and M. Zuerch, "Table-top extreme ultraviolet second harmonic generation," Sci. Adv. **7**(21), eabe2265 (2021).
153. A. M. Maiden, M. J. Humphry, and J. M. Rodenburg, "Ptychographic transmission microscopy in three dimensions using a multi-slice approach," J. Opt. Soc. Am. A **29**(8), 1606–1614 (2012).
154. E. H. R. Tsai, I. Usov, A. Diaz, A. Menzel, and M. Guizar-Sicairos, "X-ray ptychography with extended depth of field," Opt. Express **24**(25), 29089 (2016).
155. P. Li and A. Maiden, "Multi-slice ptychographic tomography," Sci. Rep. **8**(1), 2049 (2018).
156. M. Stockmar, P. Cloetens, I. Zanette, B. Enders, M. Dierolf, F. Pfeiffer, and P. Thibault, "Near-field ptychography: phase retrieval for inline holography using a structured illumination," Sci. Rep. **3**(1), 1927 (2013).
157. K. Patorski, "Fraunhofer diffraction patterns of tilted planar objects," Opt. Acta **30**(5), 673–679 (1983).
158. P. Thibault and A. Menzel, "Reconstructing state mixtures from diffraction measurements," Nature **494**(7435), 68–71 (2013).
159. D. J. Batey, D. Claus, and J. M. Rodenburg, "Information multiplexing in ptychography," Ultramicroscopy **138**, 13–21 (2014).
160. R. Röhrich, A. F. Koenderink, S. Witte, and L. Loetgering, "Spatial coherence control and analysis via micromirror-based mixed-state ptychography," New J. Phys. **23**(5), 053016 (2021).
161. A. M. Maiden, M. J. Humphry, M. C. Sarahan, B. Kraus, and J. M. Rodenburg, "An annealing algorithm to correct positioning errors in ptychography," Ultramicroscopy **120**, 64–72 (2012).
162. F. Zhang, I. Peterson, J. Vila-Comamala, A. Diaz, F. Berenguer, R. Bean, B. Chen, A. Menzel, I. K. Robinson, and J. M. Rodenburg, "Translation position determination in ptychographic coherent diffraction imaging," Opt. Express **21**(11), 13592–13606 (2013).
163. M. Odstrcil, A. Menzel, and M. Guizar-Sicairos, "Iterative least-squares solver for generalized maximum-likelihood ptychography," Opt. Express **26**(3), 3108 (2018).
164. L. Loetgering, M. Du, K. S. E. Eikema, and S. Witte, "zPIE: an autofocusing algorithm for ptychography," Opt. Lett. **45**(7), 2030 (2020).
165. C. Yang, J. Qian, A. Schirotzek, F. Maia, and S. Marchesini, "Iterative Algorithms for Ptychographic Phase Retrieval," arXiv:1105.5628 (2011).
166. P. Thibault and M. Guizar-Sicairos, "Maximum-likelihood refinement for coherent diffractive imaging," New J. Phys. **14**(6), 063004 (2012).
167. A. Maiden, D. Johnson, and P. Li, "Further improvements to the ptychographical iterative engine," Optica **4**(7), 736 (2017).
168. J. W. Goodman, *Introduction to Fourier Optics* (WH Freeman, 2017), 4th ed.
169. R. Bracewell, *The Fourier Transform and Its Applications* (Mcgraw-Hill, New York, 1999), 3rd ed.
170. D. J. Batey, T. B. Edo, C. Rau, U. Wagner, Z. D. Pešić, T. A. Waigh, and J. M. Rodenburg, "Reciprocal-space up-sampling from real-space oversampling in x-ray ptychography," Phys. Rev. A **89**(4), 043812 (2014).
171. L. Loetgering, M. Rose, D. Treffer, I. A. Vartanyants, A. Rosenhahn, and T. Wilhein, "Data compression strategies for ptychographic diffraction imaging," Adv. Opt. Technol. **6**(6), 475–483 (2017).
172. B. Enders, "Development and Application of Decoherence Models in Ptychographic Diffraction Imaging," Ph.D. thesis, Technical University Munich (2016).
173. B. Zhang, D. F. Gardner, M. D. Seaberg, E. R. Shanblatt, H. C. Kapteyn, M. M. Murnane, and D. E. Adams, "High contrast 3D imaging of surfaces near the wavelength limit using tabletop EUV ptychography," Ultramicroscopy **158**, 98–104 (2015).
174. M. Guizar-Sicairos, M. Holler, A. Diaz, J. Vila-Comamala, O. Bunk, and A. Menzel, "Role of the illumination spatial-frequency spectrum for ptychography," Phys. Rev. B **86**(10), 100103 (2012).
175. P. D. Baksh, M. Odstrčil, H.-S. Kim, S. A. Boden, J. G. Frey, and W. S. Brocklesby, "Wide-field broadband extreme ultraviolet transmission ptychography using a high-harmonic source," Opt. Lett. **41**(7), 1317 (2016).
176. A. M. Maiden, G. R. Morrison, B. Kaulich, A. Gianoncelli, and J. M. Rodenburg, "Soft X-ray spectromicroscopy using ptychography with randomly phased illumination," Nat. Commun. **4**(1), 1669 (2013).
177. G. R. Morrison, F. Zhang, A. Gianoncelli, and I. K. Robinson, "X-ray ptychography using randomized zone plates," Opt. Express **26**(12), 14915 (2018).
178. M. Odstrčil, M. Lebugle, M. Guizar-Sicairos, C. David, and M. Holler, "Towards optimized illumination for high-resolution ptychography," Opt. Express **27**(10), 14981 (2019).
179. W. Eschen, L. Loetgering, V. Schuster, R. Klas, A. Kirsche, S. Skruszewicz, L. Berthold, M. Steinert, T. Pertsch, H. Gross, M. Krause, J. Limpert, and J. Rothhardt, "Material-specific high-resolution table-top extreme ultraviolet microscopy," arXiv:2112.13046v1 (2021).
180. G. K. Tadesse, W. Eschen, R. Klas, M. Tschernajew, T. Frederik, M. Steinert, M. Zilk, V. Sch, M. Zürch, T. Pertsch, C. Spiel, J. Li, J. Rothhardt, F. Tuitje, M. Steinert, M. Zilk, V. Schuster, T. Pertsch, C. Spielmann, J. Limpert, J. Rothhardt, T. Frederik, M. Steinert, M. Zilk, V. Sch, M. Zürch, T. Pertsch, C. Spiel, J. Li, and J. Rothhardt, "Wavelength-scale ptychographic coherent diffractive imaging using a high-order harmonic source," Sci. Rep. **9**(1), 1735 (2019).

Optics EXPRESS

181. P. D. Baksh, M. Ostrčil, M. Miszczak, C. Pooley, R. T. Chapman, A. S. Wyatt, E. Springate, J. E. Chad, K. Deinhardt, J. G. Frey, and W. S. Brocklesby, "Quantitative and correlative extreme ultraviolet coherent imaging of mouse hippocampal neurons at high resolution," Sci. Adv. **6**(18), eaaz3025 (2020).
182. P. Sidorenko and O. Cohen, "Single-shot ptychography," Optica **3**(1), 9 (2016).
183. A. M. Maiden, M. J. Humphry, F. Zhang, and J. M. Rodenburg, "Superresolution imaging via ptychography," J. Opt. Soc. Am. A **28**(4), 604–612 (2011).
184. D. F. Gardner, M. Tanksalvala, E. R. Shanblatt, X. Zhang, B. R. Galloway, C. L. Porter, R. Karl Jr, C. Bevis, D. E. Adams, H. C. Kapteyn, M. M. Murnane, and G. F. Mancini, "Subwavelength coherent imaging of periodic samples using a 13.5 nm tabletop high-harmonic light source," Nat. Photonics **11**(4), 259–263 (2017).
185. C. Jacobsen, *X-ray Microscopy* (Cambridge University Press, 2019).
186. F. Seiboth, A. Schropp, M. Scholz, F. Wittwer, C. Rödel, M. Wünsche, T. Ullsperger, S. Nolte, J. Rahomäki, and K. Parfeniukas, and Others, "Perfect X-ray focusing via fitting corrective glasses to berrated optics," Nat. Commun. **8**(1), 14623 (2017).
187. M. Feser, C. Jacobsen, P. Rehak, and G. DeGeronimo, "Scanning transmission x-ray microscopy with a segmented detector," in *Journal de Physique IV (Proceedings)*, vol. 104 (EDP sciences, 2003), pp. 529–534.
188. A. M. Maiden and J. M. Rodenburg, "An improved ptychographical phase retrieval algorithm for diffractive imaging," Ultramicroscopy **109**(10), 1256–1262 (2009).
189. M. Guizar-Sicairos and J. R. Fienup, "Phase retrieval with transverse translation diversity: a nonlinear optimization approach," Opt. Express **16**(10), 7264 (2008).
190. P. Mercère, P. Zeitoun, M. Idir, S. Le Pape, D. Douillet, X. Levecq, G. Dovillaire, S. Bucourt, K. A. Goldberg, P. P. Naulleau, and S. Rekawa, "Hartmann wave-front measurement at 13.4 nm with $\lambda_E UV$/120 accuracy," Opt. Lett. **28**(17), 1534 (2003).
191. H. Medecki, E. Tejnil, K. A. Goldberg, and J. Bokor, "Phase-shifting point diffraction interferometer," Opt. Lett. **21**(19), 1526 (1996).
192. D. G. Lee, J. J. Park, J. H. Sung, and C. H. Nam, "Wave-front phase measurements of high-order harmonic beams by use of point-diffraction interferometry," Opt. Lett. **28**(6), 480 (2003).
193. D. R. Austin, T. Witting, C. A. Arrell, F. Frank, A. S. Wyatt, J. P. Marangos, J. W. Tisch, and I. A. Walmsley, "Lateral shearing interferometry of high-harmonic wavefronts," Opt. Lett. **36**(10), 1746 (2011).
194. E. Frumker, G. G. Paulus, H. Niikura, D. M. Villeneuve, and P. B. Corkum, "Frequency-resolved high-harmonic wavefront characterization," Opt. Lett. **34**(19), 3026 (2009).
195. W. Eschen, G. Tadesse, Y. Peng, M. Steinert, T. Pertsch, J. Limpert, and J. Rothhardt, "Single-shot characterization of strongly focused coherent XUV and soft X-ray beams," Opt. Lett. **45**(17), 4798–4801 (2020).
196. L. Freisem, G. S. M. Jansen, D. Rudolf, K. S. E. Eikema, and S. Witte, "Spectrally resolved single-shot wavefront sensing of broadband high-harmonic sources," Opt. Express **26**(6), 6860 (2018).
197. C. M. Kewish, P. Thibault, M. Dierolf, O. Bunk, A. Menzel, J. Vila-Comamala, K. Jefimovs, and F. Pfeiffer, "Ptychographic characterization of the wavefield in the focus of reflective hard X-ray optics," Ultramicroscopy **110**(4), 325–329 (2010).
198. M. Odstrcil, P. Baksh, S. A. Boden, R. Card, J. E. Chad, J. G. Frey, and W. S. Brocklesby, "Ptychographic coherent diffractive imaging with orthogonal probe relaxation," Opt. Express **24**(8), 8360–8369 (2016).
199. P. Thibault, M. Dierolf, O. Bunk, A. Menzel, and F. Pfeiffer, "Probe retrieval in ptychographic coherent diffractive imaging," Ultramicroscopy **109**(4), 338–343 (2009).
200. D. Spangenberg, P. Neethling, E. Rohwer, M. H. Brügmann, and T. Feurer, "Time-domain ptychography," Phys. Rev. A **91**(2), 021803 (2015).
201. D. Spangenberg, E. Rohwer, M. H. Brügmann, and T. Feurer, "Ptychographic ultrafast pulse reconstruction," Opt. Lett. **40**(6), 1002 (2015).
202. D. J. Kane and R. Trebino, "Characterization of arbitrary femtosecond pulses using frequency-resolved optical gating," IEEE J. Quantum Electron. **29**(2), 571–579 (1993).
203. P. Sidorenko, O. Lahav, Z. Avnat, and O. Cohen, "Ptychographic reconstruction algorithm for frequency-resolved optical gating: super-resolution and supreme robustness," Optica **3**(12), 1320 (2016).
204. C. Bourassin-Bouchet and M. E. Couprie, "Partially coherent ultrafast spectrography," Nat. Commun. **6**(1), 6465 (2015).
205. M. Lucchini, M. Brügmann, A. Ludwig, L. Gallmann, U. Keller, and T. Feurer, "Ptychographic reconstruction of attosecond pulses," Opt. Express **23**(23), 29502 (2015).
206. M. Lucchini, G. D. Lucarelli, M. Murari, A. Trabattoni, N. Fabris, F. Frassetto, S. De Silvestri, L. Poletto, and M. Nisoli, "Few-femtosecond extreme-ultraviolet pulses fully reconstructed by a ptychographic technique," Opt. Express **26**(6), 6771 (2018).
207. T. Witting, F. J. Furch, O. Kornilov, M. Osolodkov, C. P. Schulz, and M. J. Vrakking, "Retrieval of attosecond pulse ensembles from streaking experiments using mixed state time-domain ptychography," J. Phys. B: At., Mol. Opt. Phys. **53**(19), 194001 (2020).
208. Y. Nagata, T. Harada, T. Watanabe, H. Kinoshita, and K. Midorikawa, "At wavelength coherent scatterometry microscope using high-order harmonics for EUV mask inspection," (2019).

Optics EXPRESS

209. I. Mochi, P. Helfenstein, I. Mohacsi, R. Rajeev, D. Kazazis, S. Yoshitake, and Y. Ekinci, "RESCAN: an actinic lensless microscope for defect inspection of EUV reticles," J. Micro/Nanolithogr., MEMS, MOEMS **16**(4), 041003 (2017).
210. I. Mochi, S. Fernandez, R. Nebling, U. Locans, R. Rajeev, A. Dejkameh, D. Kazazis, L.-T. Tseng, S. Danylyuk, L. Juschkin, and Y. Ekinci, "Quantitative characterization of absorber and phase defects on EUV reticles using coherent diffraction imaging," J. Micro/Nanolithogr., MEMS, MOEMS **19**(01), 1 (2020).
211. E. R. Shanblatt, C. L. Porter, D. F. Gardner, G. F. Mancini, R. M. Karl, M. D. Tanksalvala, C. S. Bevis, V. H. Vartanian, H. C. Kapteyn, D. E. Adams, and M. M. Murnane, "Quantitative Chemically Specific Coherent Diffractive Imaging of Reactions at Buried Interfaces with Few Nanometer Precision," Nano Lett. **16**(9), 5444–5450 (2016).
212. R. M. Karl, G. F. Mancini, J. L. Knobloch, T. D. Frazer, J. N. Hernandez-Charpak, B. Abad, D. F. Gardner, E. R. Shanblatt, M. Tanksalvala, C. L. Porter, C. S. Bevis, D. E. Adams, H. C. Kapteyn, and M. M. Murnane, "Full-field imaging of thermal and acoustic dynamics in an individual nanostructure using tabletop high harmonic beams," Sci. Adv. **4**(10), eaau4295 (2018).
213. G. F. Mancini, R. M. Karl, E. R. Shanblatt, C. S. Bevis, D. F. Gardner, M. D. Tanksalvala, J. L. Russell, D. E. Adams, H. C. Kapteyn, J. V. Badding, T. E. Mallouk, and M. M. Murnane, "Colloidal crystal order and structure revealed by tabletop extreme ultraviolet scattering and coherent diffractive imaging," Opt. Express **26**(9), 11393 (2018).
214. A. Leblanc, S. Monchocé, C. Bourassin-Bouchet, S. Kahaly, and F. Quéré, "Ptychographic measurements of ultrahigh-intensity laser–plasma interactions," Nat. Phys. **12**(4), 301–305 (2016).
215. F. Tuitje, P. Martínez Gil, T. Helk, J. Gautier, F. Tissandier, J.-P. Goddet, A. Guggenmos, U. Kleineberg, S. Sebban, E. Oliva, C. Spielmann, and M. Zürch, "Nonlinear ionization dynamics of hot dense plasma observed in a laser-plasma amplifier," Light: Sci. Appl. **9**(1), 187 (2020).
216. M. Uchida, G. McDermott, M. Wetzler, M. A. Le Gros, M. Myllys, C. Knoechel, A. E. Barron, and C. A. Larabell, "Soft X-ray tomography of phenotypic switching and the cellular response to antifungal peptoids in Candida albicans," Proc. Natl. Acad. Sci. U. S. A. **106**(46), 19375–19380 (2009).
217. H. M. Hertz, O. von Hofsten, M. Bertilson, U. Vogt, A. Holmberg, J. Reinspach, D. Martz, M. Selin, A. E. Christakou, J. Jerlström-Hultqvist, and S. Svärd, "Laboratory cryo soft X-ray microscopy," J. Struct. Biol. **177**(2), 267–272 (2012).
218. K. Giewekemeyer, M. Beckers, T. Gorniak, M. Grunze, T. Salditt, and A. Rosenhahn, "Ptychographic coherent x-ray diffractive imaging in the water window," Opt. Express **19**(2), 1037–1050 (2011).
219. T. Popmintchev, M. C. Chen, A. Bahabad, M. Gerrity, P. Sidorenko, O. Cohen, I. P. Christov, M. M. Murnane, and H. C. Kapteyn, "Phase matching of high harmonic generation in the soft and hard X-ray regions of the spectrum," Proc. Natl. Acad. Sci. U. S. A. **106**(26), 10516–10521 (2009).
220. T. Popmintchev, M. C. Chen, D. Popmintchev, P. Arpin, S. Brown, S. Ališauskas, G. Andriukaitis, T. Balčiunas, O. D. Mücke, A. Pugzlys, A. Baltuška, B. Shim, S. E. Schrauth, A. Gaeta, C. Hernández-García, L. Plaja, A. Becker, A. Jaron-Becker, M. M. Murnane, and H. C. Kapteyn, "Bright coherent ultrahigh harmonics in the kev x-ray regime from mid-infrared femtosecond lasers," Science **336**(6086), 1287–1291 (2012).
221. C. L. Porter, M. Tanksalvala, M. Gerrity, G. Miley, X. Zhang, C. Bevis, E. Shanblatt, R. Karl, M. M. Murnane, D. E. Adams, and H. C. Kapteyn, "General-purpose, wide field-of-view reflection imaging with a tabletop 13 nm light source," Optica **4**(12), 1552 (2017).
222. W. Eschen, V. Schuster, S. Wang, L. Loetgering, C. Liu, R. Klas, J. Limpert, and J. Rothhardt, "Ultrafast nanoscale XUV table-top coherent diffractive imaging," in *Frontiers in Ultrafast Optics: Biomedical, Scientific, and Industrial Applications XXI*, vol. 11676 (International Society for Optics and Photonics, 2021), p. 116761B.
223. M. Dierolf, A. Menzel, P. Thibault, P. Schneider, C. M. Kewish, R. Wepf, O. Bunk, and F. Pfeiffer, "Ptychographic X-ray computed tomography at the nanoscale," Nature **467**(7314), 436–439 (2010).
224. M. Holler, A. Diaz, M. Guizar-Sicairos, P. Karvinen, E. Färm, E. Härkönen, M. Ritala, A. Menzel, J. Raabe, and O. Bunk, "X-ray ptychographic computed tomography at 16 nm isotropic 3D resolution," Sci. Rep. **4**(1), 3857 (2015).
225. M. Holler, M. Guizar-Sicairos, E. H. R. Tsai, R. Dinapoli, E. Müller, O. Bunk, J. Raabe, and G. Aeppli, "High-resolution non-destructive three- dimensional imaging of integrated circuits," Nature **543**(7645), 402–406 (2017).
226. T. M. Godden, R. Suman, M. J. Humphry, J. M. Rodenburg, and A. M. Maiden, "Ptychographic microscope for three-dimensional imaging," Opt. Express **22**(10), 12513 (2014).
227. M. Du, L. Loetgering, K. S. E. Eikema, and S. Witte, "Ptychographic optical coherence tomography," Opt. Lett. **46**(6), 1337 (2021).
228. K. C. Zhou, R. Qian, A.-H. Dhalla, S. Farsiu, and J. A. Izatt, "Unified k-space theory of optical coherence tomography," Adv. Opt. Photonics **13**(2), 462–514 (2021).
229. S. Fuchs, A. Blinne, C. Rödel, U. Zastrau, V. Hilbert, M. Wünsche, J. Bierbach, E. Frumker, E. Förster, and G. G. Paulus, "Optical coherence tomography using broad-bandwidth XUV and soft X-ray radiation," Appl. Phys. B **106**(4), 789–795 (2012).
230. S. Fuchs, C. Rödel, A. Blinne, U. Zastrau, M. Wünsche, V. Hilbert, L. Glaser, J. Viefhaus, E. Frumker, and P. Corkum, and Others, "Nanometer resolution optical coherence tomography using broad bandwidth XUV and soft x-ray radiation," Sci. Rep. **6**(1), 20658 (2016).

Optics EXPRESS

231. S. Fuchs, M. Wünsche, J. Nathanael, J. J. Abel, C. Rödel, J. Biedermann, J. Reinhard, U. Hübner, and G. G. Paulus, "Optical coherence tomography with nanoscale axial resolution using a laser-driven high-harmonic source," Optica **4**(8), 903–906 (2017).
232. F. Wiesner, M. Wünsche, J. Reinhard, J. J. Abel, J. Nathanael, S. Skruszewicz, C. Rödel, S. Yulin, A. Gawlik, G. Schmidl, U. Hübner, J. Plentz, G. G. Paulus, and S. Fuchs, "Material-specific imaging of nanolayers using extreme ultraviolet coherence tomography," Optica **8**(2), 230 (2021).